


Spin winding and topological nature of transitions in the Jaynes-Cummings model with Stark nonlinear coupling

Zu-Jian Ying *

*School of Physical Science and Technology, Lanzhou University, Lanzhou 730000, China
and Key Laboratory for Quantum Theory and Applications of MoE, Lanzhou Center for Theoretical Physics, and
Key Laboratory of Theoretical Physics of Gansu Province, Lanzhou University, Lanzhou, Gansu 730000, China*

 (Received 28 August 2023; revised 4 December 2023; accepted 27 March 2024; published 3 May 2024)

Besides exploring novel transition patterns, acquiring a full understanding of the transition nature is an ultimate pursuit in studies of phase transitions. The fundamental models of light-matter interactions manifest single-qubit topological phase transitions (TPTs), which call for an analytical demonstration apart from numerical studies. We present a rigorous study of TPTs in the Jaynes-Cummings model generally with Stark nonlinear coupling. In terms of the properties of Hermite polynomials, we show that the topological structure of the eigenfunction has an exact correspondence to the spin winding by nodes, which yields a full spin winding without antiwinding nodes. We find it is the superposition between neighboring Fock states that leads to such a nontrivial spin winding. The spurious fractional contribution to the winding number of the winding angle at infinity is found to be actually an integer. Thus, the phase transitions in the model have the nature of TPTs and the excitation number is endowed as a topological quantum number. The principal transition establishes a paradigmatic case in which a transition is of both the symmetry-breaking Landau class of transition and the symmetry-protected topological class of transition, while conventionally these two classes of transitions are incompatible due to the contrary symmetry requirements. Such a transition-class reconciliation is realized by a preserved higher symmetry (here the parity) which protects the TPTs, while the symmetry breaking involves the subsymmetries. We also explain the origin of unconventional TPTs in the presence of counterrotating terms. Our results may provide deeper insight into the few-body phase transitions in light-matter interactions.

DOI: [10.1103/PhysRevA.109.053705](https://doi.org/10.1103/PhysRevA.109.053705)

I. INTRODUCTION

Recent years have witnessed both theoretical progress [1–4] and experimental advances [5–19] in the frontier of light-matter interactions. In this context, especially with the entrance into the era of ultrastrong [5–18] and deep-strong [18,19] couplings, few-body quantum phase transitions (QPTs) have become practically relevant and have attracted particular attention [4,20–32] among the massive efforts [1–6,20–87] in the dialogue between mathematics and physics [2] inspired by the milestone of finding integrability of the fundamental light-matter-interaction model [1]. Few-body QPTs are fascinating not only because they exhibit critical and universal behaviors [22–25,28,30] as in many-body systems [24,25] but also due to their high controllability and tunability, which show advantages in applications such as in quantum metrology [51–54].

Phase transition (PT) is a ubiquitous phenomenon in our physical world. Whereas investigation of PTs is a field full of challenges, also surprising discoveries may be often encountered. Exploring novel patterns of PTs and seeking a full understanding of PTs have always been goals. In this regard, the well-known Landau theory [88] made a breakthrough in understanding traditional phase transitions by realizing that a

PT is associated with some symmetry breaking, while another essentially different class of PT is the topological phase transition (TPT) [89–94], which does not break the symmetry of the system. Phase transitions are also classified into classical ones and quantum ones; the former are thought to be driven by thermal fluctuations and the latter by quantum fluctuations [24,95]. Since the symmetry requirement of these two classes of PTs are contrary, they are in principle incompatible. An exceptional finding of their coexistence would be surprising and intriguing.

When PTs traditionally occur in thermodynamical systems, few-body systems can also manifest PTs, as it has been found in light-matter interactions. Indeed, the quantum Rabi model (QRM) [40,96,97], known as the most fundamental model of light-matter interactions, possesses a QPT [20–22] in the low-frequency limit $\omega/\Omega \rightarrow 0$ for the ratio of the bosonic mode frequency ω and the atomic level splitting Ω , which is a replacement for the thermodynamical limit in many-body systems. At this point, as a mutual support from other fields, it is worth mentioning that finite-size PTs can also occur with level crossings in pairing-depairing models [98–100] and coupled fermion-boson models [101–103] realizable in superconducting [99,100,102] and cold atomic systems [98,99,103]. Although it might be a matter of preference whether to term the transition quantum by considering the negligible quantum fluctuations in the photon vacuum state [24], the transition in the QRM is found to have

*yingzj@lzu.edu.cn

scaling behavior which forms critical universality as in traditional QPTs. Such critical universality not only valid for anisotropy [25,28], but also holds for the Stark nonlinear coupling [30] and the critical exponents can be bridged to the thermodynamical case [25]. On the other hand, apart from the various patterns of explicit [27] or hidden [28] symmetry breaking as in the Landau class of PTs, the symmetry-protected TPTs also emerge [28–31] in these single-qubit systems (see a brief comparison of TPTs and Landau-class PTs in Appendix A). Interestingly, these TPTs not only occur at gap closing [28–31] as in the conventional TPTs in condensed matter [93,104–109], but also happen in gapped situations [29–31] analogously to the unconventional TPTs in the quantum spin Hall effect with strong electron-electron interactions [110] and the quantum anomalous Hall effect with disorder [111]. The study extending topological transitions to excited states in the presence of level anticrossing also reveals other unconventional types of TPTs with unmatched wave-function nodes and spin-winding numbers, as well as topological transitions of spin knots [31]. However, these studies on the single-qubit TPTs are based on numerical analysis; a more convincing analytical study is lacking. In such a situation, the problem of the winding angle at infinity remains elusive and unconventional TPTs are in need of a clearer understanding [31].

In this work we present a rigorous study of topological transitions in a fundamental model of light-matter interactions generally including the Jaynes-Cummings (JC) linear coupling [83,112] and Stark nonlinear coupling [30,41–43] (JC-Stark model). As the eigenstates are composed of two Hermite polynomials, we rigorously demonstrate that the topological structure of the wave function has an exact correspondence to the spin winding by nodes and that the spin is winding without antiwinding nodes. We also analytically show that the spurious fractional contribution of the winding angle at infinity to the winding number is actually an integer. Thus, the PTs in the model have the nature of TPTs and the excitation number is endowed the connotation of a topological quantum number. We also point out that the principal transition is simultaneously of both the symmetry-breaking Landau class of transition and the symmetry-protected topological class of transition, while conventionally these two classes of transitions are incompatible due to the contrary symmetry requirements. Our results may provide deeper insight into the few-body phase transitions in light-matter interactions, including the origin of unconventional topological transitions.

The paper is organized as follows. Section II introduces the JC-Stark model for analytical analysis in this work. Anisotropy is also included for further discussion. Section III presents the exact solution of the JC-Stark model. Section IV shows the topological nature of the transitions by analytical analysis of the nodes of the eigenfunctions and the correspondence of spin windings. Section V demonstrates that the principal transition is simultaneously both a Landau-class and topological-class transition. Section VI shows the TPTs without parity variation and gives an understanding of the unconventional TPTs without gap closing for the anisotropic case. Section VII provides a summary and discusses our conclusions.

II. MODEL AND SYMMETRY

We start with a fundamental model of light-matter interactions with the Hamiltonian [30,85]

$$H = H_0 + H_g + H_\lambda + H_{\text{Stark}}, \quad (1)$$

$$H_0 = \omega a^\dagger a + \frac{\Omega}{2} \sigma_x, \quad H_{\text{Stark}} = \chi \omega \hat{n} \sigma_x, \quad (2)$$

$$H_g = g(\tilde{\sigma}_- a^\dagger + \tilde{\sigma}_+ a), \quad H_\lambda = \lambda g(\tilde{\sigma}_+ a^\dagger + \tilde{\sigma}_- a), \quad (3)$$

which generally includes a bosonic mode with photon number $\hat{n} = a^\dagger a$ and frequency ω , a qubit represented by the Pauli matrices $\sigma_{x,y,z}$ with level splitting Ω , the rotating-wave term of interaction H_g with coupling strength g , the counterrotating term H_λ with coupling anisotropy ratio λ , and the Stark nonlinear interaction [41–43] H_{Stark} with coupling ratio χ . In the literature, $H_{\text{JC}} = H_0 + H_g$ is the Jaynes-Cummings model (JCM) [83,112], $H_0 + H_g + H_\lambda$ is the anisotropic QRM [45], and the $\lambda = 1$ case is the QRM [40,96,97]. Here we define $\tilde{\sigma}_\pm = (\sigma_z \mp i\sigma_y)/2$ adopting the spin notation as in Ref. [39], in which $\sigma_z = \pm$ conveniently represents the two flux states in the flux-qubit circuit system [113]. The tilde of $\tilde{\sigma}_\pm$ denotes spin raising and lowering on the σ_x basis, to distinguish the later-defined σ_\pm on the σ_z basis. We can retrieve the conventional notation by a spin rotation $\{\sigma_x, \sigma_y, \sigma_z\} \rightarrow \{\sigma_z, -\sigma_y, \sigma_x\}$ around the axis $\vec{x} + \vec{z}$. Numerical studies show that these models manifest single-qubit TPTs [28–31]. In the present work, for our analytical investigation, we first focus on the JC-Stark model [30]

$$H_{\text{JC-Stark}} = H_0 + H_g + H_{\text{Stark}}. \quad (4)$$

Ultimately, we will also use the analytical results to discuss the unconventional TPTs in the general model H . All these models have parity symmetry $[\hat{P}, H] = 0$, with $\hat{P} = \sigma_x(-1)^{a^\dagger a}$, which as we will see is the key symmetry that protects the TPTs.

To extract the topological feature we rewrite the Hamiltonian in position space

$$H = \frac{\omega}{2} \hat{p}^2 + v_{\sigma_z}(x) + H_+ \sigma_+ + H_- \sigma_-, \quad (5)$$

$$H_\pm = \frac{\Omega - \chi\omega}{2} \mp g_y i\sqrt{2} \hat{p} + \frac{\chi\omega}{2} (\hat{x}^2 + \hat{p}^2), \quad (6)$$

with the substitutions $a^\dagger = (\hat{x} - i\hat{p})/\sqrt{2}$ and $a = (\hat{x} + i\hat{p})/\sqrt{2}$, where $\hat{p} = -i\frac{\partial}{\partial x}$, and spin raising and lowering on the $\sigma_z = \pm$ basis, i.e., $\sigma_x = \sigma_+ + \sigma_-$ and $\sigma_y = -i(\sigma_+ - \sigma_-)$. In such a representation $v_{\sigma_z}(x) = \omega(x + g'_z \sigma_z)^2/2 + \varepsilon_0^z$ is an effective spin-dependent potential with $g'_z = \sqrt{2}g_z/\omega$, $g_z = \frac{1+\lambda}{2}g$, and $\varepsilon_0^z = -\frac{1}{2}(g_z^2 + 1)\omega$. The Ω term now acts as spin flipping in σ_z space or tunneling in position space [21,39]. We also define $g_y = \frac{1-\lambda}{2}g$. The g_y terms, together as $\sqrt{2}g_y \hat{p} \sigma_y$, resemble [30] the Rashba spin-orbit coupling in nanowires [114–118] or the equal-weight mixture [29,119,120] of the linear Dresselhaus [121] and Rashba [122] spin-orbit couplings.

III. EXACT SOLUTION

The JC-Stark model (4) possesses U(1) symmetry, as denoted by the excitation number $\hat{n} + |\uparrow\rangle\langle\uparrow|$ or

$\hat{n} + \sigma_x/2 + 1/2$; the eigenstates only involve bases with the same excitation number n and take the following form [30], similar to the JCM [83,112]:

$$\psi_n^{(x,\eta)} = (C_{n\uparrow}^{(\eta)}|n-1, \uparrow\rangle + C_{n\downarrow}^{(\eta)}|n, \downarrow\rangle)/\sqrt{N_n}, \quad (7)$$

$$\psi_0 = |0, \downarrow\rangle. \quad (8)$$

Here $\eta = \pm$ denotes two branches of energy levels, $n = 1, 2, \dots$ labels the Fock state on the photon-number basis, and \uparrow and \downarrow are two spin states of σ_x . The parity is negative (positive) when n is even (odd):

$$\hat{P}\psi_n^{(x,\eta)} = (-1)^{n-1}\psi_n^{(x,\eta)}, \quad \hat{P}\psi_0 = (-1)\psi_0. \quad (9)$$

The coefficients are explicitly given by

$$C_{n\uparrow}^{(\eta)} = e_- + \eta\sqrt{e_-^2 + n g^2}, \quad (10)$$

$$C_{n\downarrow}^{(\eta)} = g\sqrt{n}, \quad (11)$$

where $e_+ = (n - \frac{1+\chi}{2})\omega$, $e_- = \frac{1}{2}(\Omega - \omega) + (n - \frac{1}{2})\chi\omega$, and $N_n = C_{n\uparrow}^{(\eta)2} + C_{n\downarrow}^{(\eta)2}$ is the normalization factor. For state ψ_0 we can define $C_{0\downarrow} = 1$ and $C_{0\uparrow} = 0$ using similar coefficient notation. Correspondingly, the eigenenergies are determined by

$$E^{(n,\eta)} = e_+ + \eta\sqrt{e_-^2 + n g^2}, \quad (12)$$

$$E^0 = -\frac{\Omega}{2}. \quad (13)$$

Apparently, the energy branch $E^{(n,+)}$ is higher than $E^{(n,-)}$; thus the ground state is the lowest state of $\psi_n^{(x,-)}$ and ψ_0 . So far n is only the excitation number and we have not seen any topological aspect.

IV. TOPOLOGICAL-TRANSITION NATURE AT FINITE FREQUENCIES

A. Wave-function nodes

Corresponding to Eq. (7), we can rewrite the eigenfunctions in position space

$$\psi_+^x(x) \equiv \psi_{n,\uparrow}^{(x,\eta)}(x) = C_{n\uparrow}^{(\eta)}\phi_{n-1}(x)/\sqrt{N_n}, \quad (14)$$

$$\psi_-^x(x) \equiv \psi_{n,\downarrow}^{(x,\eta)}(x) = C_{n\downarrow}^{(\eta)}\phi_n(x)/\sqrt{N_n}, \quad (15)$$

where $\phi_n(x) = \langle x|n\rangle$ is the eigenfunction of the quantum harmonic oscillator with quantum number n ,

$$\phi_n(x) = \frac{1}{\pi^{1/4}\sqrt{2^n n!}} H_n(x) e^{-x^2/2}. \quad (16)$$

Note that the Hermite polynomial $H_n(x)$ has a number n of real roots $x = y_Z$, where $H_n(y_Z) = 0$. Accordingly, the wave-function components $\psi_{n,\uparrow}^{(x,\eta)}(x)$ and $\psi_{n,\downarrow}^{(x,\eta)}(x)$ have $n-1$ and n real nodes y_Z , respectively, where $\psi_{n,\sigma_x}^{(x,\pm)}(y_Z) = 0$.

We can also transform onto the spin- σ_z basis, represented by \uparrow and \downarrow , on which the wave function becomes

$$\psi_n^{(z,\eta)} = \psi_+^z(x)|\uparrow\rangle + \psi_-^z(x)|\downarrow\rangle, \quad (17)$$

with spin components

$$\psi_+^z(x) \equiv \psi_{n,\uparrow}^{(z,\eta)}(x) = \frac{C_{n\uparrow}^{(\eta)}\phi_{n-1}(x) + C_{n\downarrow}^{(\eta)}\phi_n(x)}{\sqrt{2N_n}}, \quad (18)$$

$$\psi_-^z(x) \equiv \psi_{n,\downarrow}^{(z,\eta)}(x) = \frac{C_{n\uparrow}^{(\eta)}\phi_{n-1}(x) - C_{n\downarrow}^{(\eta)}\phi_n(x)}{\sqrt{2N_n}}. \quad (19)$$

The parity symmetry ensures

$$\psi_{n,\uparrow}^{(z,\eta)}(x) = (-1)^{n-1}\psi_{n,\downarrow}^{(z,\eta)}(-x). \quad (20)$$

Later on in Sec. **IV D** we will see that both components have n nodes $x = x_Z$, where $\psi_{n,\sigma_z}^{(z,\eta)}(x_Z) = 0$.

We give an example of the eigenfunction in Figs. 1(a)–1(c) for $n = 6$ with $\psi_{\pm}^{x,z}(x)$ representing $\psi_{n,\sigma_x}^{(x,\eta)}(x)$ and $\psi_{n,\sigma_z}^{(z,\eta)}(x)$ in Eqs. (14), (15), (18), and (19). The nodes of $\psi_{\pm}^x(x)$ are marked by open squares (spin up $=\uparrow$) and closed squares (spin down $=\downarrow$) in Fig. 1(a) and the nodes of $\psi_{\pm}^z(x)$ by open circles (spin up $=\uparrow$) and closed circles (spin down $=\downarrow$) in Fig. 1(b). We can also plot all the nodes together in the wave-function amplitude $|\psi_{\pm}^z(x)|$ as in Fig. 1(c), where the nodes of $\psi_{n,\sigma_x}^{(x,\eta)}(x)$ are located at points $|\psi_+^z(x)| = |\psi_-^z(x)|$. Here the open squares (\uparrow) are crossing points of $\psi_+^z(x) = \psi_-^z(x)$ of both solid lines ($\psi_{\pm}^z > 0$) or both dashed lines ($\psi_{\pm}^z < 0$), while closed squares (\downarrow) are crossing points of $\psi_+^z(x) = -\psi_-^z(x)$ between solid lines and dashed lines.

The node number represents the topological structure of the wave function in the sense that with a fixed node number one cannot go to another node state by continuous shape deformation of the wave function, just as one cannot change a torus into a sphere by a continuous deformation in the topological picture of so-called rubber-sheet geometry. Such a wave-function topological structure can be reflected by the physical topological character as there is a one-to-one correspondence between the wave-function nodes and the spin-winding nodes, as we discuss in the following sections.

B. Spin winding: Node correspondence to wave-function and symmetric and antisymmetric properties

Note that the eigenfunctions in (7) and (8) are real, so the corresponding spin textures are related to the wave function components by

$$\langle\sigma_z(x)\rangle = \psi_+^z(x)^2 - \psi_-^z(x)^2 = 2\psi_+^x(x)\psi_-^x(x), \quad (21)$$

$$\langle\sigma_x(x)\rangle = \psi_+^x(x)^2 - \psi_-^x(x)^2 = 2\psi_+^z(x)\psi_-^z(x), \quad (22)$$

$$\langle\sigma_y(x)\rangle = i[\psi_-^z(x)^*\psi_+^z(x) - \psi_+^z(x)^*\psi_-^z(x)] = 0. \quad (23)$$

We see the spins are winding within the $\langle\sigma_z(x)\rangle$ - $\langle\sigma_x(x)\rangle$ plane and the nodes of the eigenfunction are in one-to-one correspondence to the nodes of the spin winding:

$$\psi_{n,\sigma_z}^{(z,\eta)}(x_Z) = 0 \iff \langle\sigma_z(x_Z)\rangle = 0, \quad (24)$$

$$\psi_{n,\sigma_x}^{(x,\eta)}(y_Z) = 0 \iff \langle\sigma_x(y_Z)\rangle = 0. \quad (25)$$

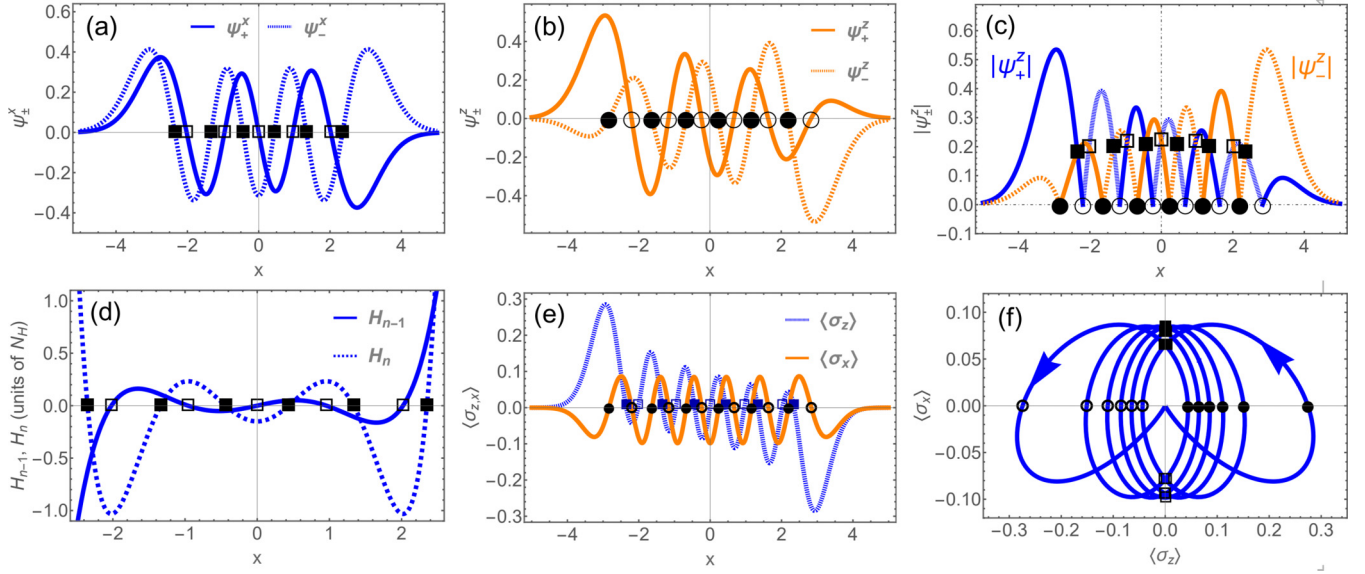


FIG. 1. Analytical correspondence of nodes or zeros in (a)–(c) wave function components, (d) Hermite polynomials, and (e) and (f) spin windings. The closed (open) squares mark the corresponding nodes in ψ_{\pm}^x (ψ_{\pm}^z), $\langle \sigma_z(x) \rangle$ with positive (negative) $\langle \sigma_x(x) \rangle$, and H_n (H_{n-1}), respectively, while closed (open) circles denote the nodes in ψ_{\pm}^z (ψ_{\pm}^x) and $\langle \sigma_x(x) \rangle$ with positive (negative) $\langle \sigma_z(x) \rangle$. Nodes of ψ_{\pm}^z (ψ_{\pm}^x) are also the amplitude-crossing points $|\psi_{\pm}^z| = |\psi_{\pm}^z|$ ($|\psi_{\pm}^x| = |\psi_{\pm}^x|$) as in (c). Here $\omega = 0.5\Omega$, $g = 2.5g_s$, $\chi = 0$, $n = 6$, and $g_s = \sqrt{\omega\Omega}/2$.

The node correspondence of the wave function and the spin winding is shown in Figs. 1(a)–1(c) and Figs. 1(e) and 1(f), respectively, where the squares represent the corresponding nodes of ψ_{\pm}^x and $\langle \sigma_z(x) \rangle$ and the circles locate the corresponding nodes of ψ_{\pm}^z and $\langle \sigma_x(x) \rangle$.

From Eqs. (21)–(23) the spin textures for state $\psi_n^{(x,\eta)}$ can be analytically obtained to be

$$\langle \sigma_z(x) \rangle = \frac{e^{-x^2} g C_{n\omega\eta}}{2^{n-3/2} N_{\sigma}} H_{n-1}(x) H_n(x), \quad (26)$$

$$\langle \sigma_x(x) \rangle = \frac{e^{-x^2}}{2^n N_{\sigma}} [C_{n\omega\eta}^2 H_{n-1}(x)^2 - 2g^2 H_n(x)^2], \quad (27)$$

$$\langle \sigma_y(x) \rangle = 0, \quad (28)$$

where $N_{\sigma} = \sqrt{\pi}(n-1)! [4g^2n + C_{n\omega\eta}\Omega_{n\omega\chi}]$, $C_{n\omega\eta} = \Omega_{n\omega\chi} + \eta\sqrt{\Omega_{n\omega\chi}^2 + 4g^2n}$, and $\Omega_{n\omega\chi} = \Omega - \omega + (2n-1)\chi\omega$. For state ψ_0 , we have $\langle \sigma_z(x) \rangle = \langle \sigma_y(x) \rangle = 0$ and $\langle \sigma_x(x) \rangle = -e^{-x^2}/\sqrt{\pi}$. Equations (26) and (27) indicate that there is also a correspondence of the roots of the Hermite polynomials to the nodes of the wave function and the spin winding, as illustrated in Fig. 1(d). This will be discussed further around Eq. (30) in Sec. IV C and with f_{\pm} in Sec. IV D.

The parity symmetry also leads to the symmetry of $\langle \sigma_x(x) \rangle$ and antisymmetry of $\langle \sigma_z(x) \rangle$. Indeed, the parity symmetry implies that $\psi_{\pm}^z(x) = P\psi_{\pm}^z(-x)$ [27], the substitution of which into (21) and (22) yields

$$\langle \sigma_z(-x) \rangle = -\langle \sigma_z(x) \rangle, \quad \langle \sigma_x(-x) \rangle = +\langle \sigma_x(x) \rangle. \quad (29)$$

The above symmetric and antisymmetric properties of $\langle \sigma_x(x) \rangle$ and $\langle \sigma_z(x) \rangle$ can also be directly seen from (26) and (27) as $H_n(-x) = (-1)^n H_n(x)$. Figure 1(e) shows an example of the spin texture. We can see that indeed $\langle \sigma_x(x) \rangle$ is symmetric and

$\langle \sigma_z(x) \rangle$ is antisymmetric, which yields a $\langle \sigma_z(x) \rangle$ reflection-symmetric spin winding in the $\langle \sigma_z(x) \rangle$ - $\langle \sigma_x(x) \rangle$ plane as demonstrated in Fig. 1(f). These symmetry properties of the spin texture will be used in the argument for the distribution of $\langle \sigma_x(x) \rangle$ nodes.

C. Invariant $\langle \sigma_z(x) \rangle$ nodes

From Eq. (26) we see that the nodes of $\langle \sigma_z(x) \rangle$ are completely determined by the roots of $H_{n-1}(x)$ and $H_n(x)$. The $\langle \sigma_z(x) \rangle$ nodes are located at the roots of the Hermite polynomials

$$H_{n-1}(z_Z^{(n-1)}) = 0 \text{ or } H_n(z_Z^{(n)}) = 0, \quad (30)$$

which are independent of the model parameters. Such an invariant feature may provide some particular advantage in designing potential topological devices. For example, these spin nodes could provide topological information for quantum topological encoding and decoding [31]. The topological information based on such an invariant node will be robust as it is completely unaffected by the variations of the parameters within the topological phase.

On the other hand, unlike the local order parameters in traditional phase transitions, the topological feature is a global property that in principle needs measurements over a global space (typically in the real space, the momentum space, or the energy spectrum space) to distinguish [108,123–125], which is a common experimental difficulty for TPTs in condensed matter. In this regard, the invariant nodes here also greatly reduce the experimental cost and simplify the identification of the topological states in experimental simulations as one only needs to check the feature around the fixed points of nodes instead of scanning a large range of x space.

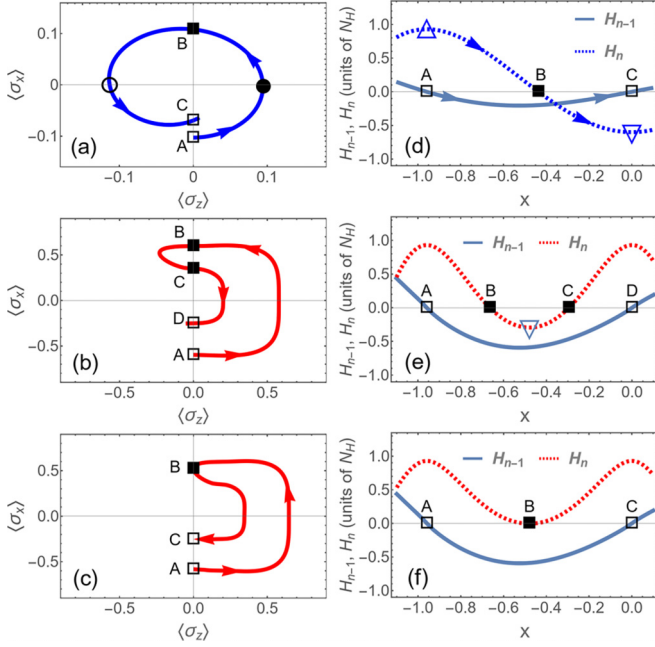


FIG. 2. Full winding without antiwinding nodes. The schematic spin winding is shown between two adjacent nodes (open squares) on the negative $\langle\sigma_x(x)\rangle$ axis, (a) without antiwinding nodes, (b) with two antiwinding nodes (closed squares) on the positive $\langle\sigma_x(x)\rangle$ axis, and (c) with one antiwinding node. The required evolution of the Hermite polynomial $H_n(x)$ (dotted lines) is shown for two adjacent roots (open squares) in $H_{n-1}(x)$, corresponding to (a)–(c), with (d) fulfilled by the Hermite polynomial properties but (e) and (f) unfulfilled.

D. Full winding without antiwinding nodes

It should be noted that the Hermite polynomial roots $z_Z^{(n-1)}$ and $z_Z^{(n)}$ alternate due to the relation

$$H'_n(x) \equiv \partial_x H_n(x) = 2nH_{n-1}(x), \quad (31)$$

which indicates that the H_{n-1} roots $z_Z^{(n-1)}$ are always the maxima or minima of $H_n(x)$, as shown by the upward and downward triangles in Fig. 2(d). From the relation $H_n(x) = 2xH_{n-1}(x) - \partial_x H_{n-1}(x)$ we see that

$$H_n(z_Z^{(n-1)}) = -H'_{n-1}(z_Z^{(n-1)}), \quad (32)$$

which indicates that two adjacent roots $z_{Z,j}^{(n-1)}$ and $z_{Z,j+1}^{(n-1)}$ must have different signs of H_n due to the different gradient signs from H'_{n-1} , i.e.,

$$H_n(z_{Z,j}^{(n-1)})H_n(z_{Z,j+1}^{(n-1)}) < 0, \quad (33)$$

leading to a root $z_Z^{(n)}$ between $z_{Z,j}^{(n-1)}$ and $z_{Z,j+1}^{(n-1)}$. [Note that here $H_n(z_{Z,j}^{(n-1)})$ and $H_n(z_{Z,j+1}^{(n-1)})$ are always finite due to the Turán inequality $H_n(x)^2 - H_{n-1}(x)H_{n+1}(x) > 0$, which excludes simultaneous zeros of $H_n(x)$ and $H_{n-1}(x)$.] Figure 2(d) shows such a case schematically: The open squares A and C represent the two adjacent H_{n-1} roots, at which the gradient has different signs, as indicated by the arrow orientations along the solid line. The H_n signs at A and C are different (indicated

by the triangles), which must surround an H_n root (closed square B).

Note that from Eqs. (26) and (27) we find H_{n-1} roots and H_n roots correspond to $\langle\sigma_z(x)\rangle$ nodes on opposite $\langle\sigma_x(x)\rangle$ axes, as in Fig. 2(a). Thus, the above analysis means that between two adjacent $\langle\sigma_z(x)\rangle$ nodes on the same $\langle\sigma_x(x)\rangle$ axis (open squares A and C) there must be another $\langle\sigma_z(x)\rangle$ node on the opposite $\langle\sigma_x(x)\rangle$ axis (closed square B). The possibility to have more than one $\langle\sigma_z(x)\rangle$ node on the opposite $\langle\sigma_x(x)\rangle$ axis as in Fig. 2(b) is excluded, as that would spuriously introduce some new H_n maximum or minimum which however has no match with H_{n-1} zero, violating the relation (31), as denoted by the triangle in Fig. 2(e). This excluded case in Fig. 2(b) also avoids antiwinding (i.e., cancellation of the spin-winding angle in the returning route). The antiwinding at one $\langle\sigma_z(x)\rangle$ node as in Fig. 2(c) is also violating the relation (31). Therefore, the $\langle\sigma_z(x)\rangle$ nodes should appear alternately on positive and negative $\langle\sigma_x(x)\rangle$ axes without antiwinding.

The same happens for $\langle\sigma_x(x)\rangle$ nodes. Actually, Eq. (27) can be factorized into a product of factors $f_{\pm} = H_{n-1}(x) \pm cH_n(x)$, where c is a parameter-determined coefficient. The $\langle\sigma_x(x)\rangle$ nodes are just the f_{\pm} roots. Both factors f_{\pm} have n roots as $H_{n-1}(x)$ and $H_n(x)$, subject to the relation (31), are interlacing with alternate zeros as in Fig. 1(d), while the number of the f_{\pm} roots is determined by the crossing times of $H_{n-1}(x)$ and $H_n(x)$, which are unaffected by any amplitude amplification with nonzero c , as one can recognize from Fig. 2(d). Thus, there are $2n$, $\langle\sigma_x(x)\rangle$ nodes, while from Eq. (27) we know there are $2n - 1$, $\langle\sigma_z(x)\rangle$ nodes. Since there is no antiwinding, the $\langle\sigma_x(x)\rangle$ nodes and the $\langle\sigma_z(x)\rangle$ nodes are also interlacing. Indeed, except for the node on the infinity side, each $\langle\sigma_x(x)\rangle$ node can only appear in the interval between two adjacent $\langle\sigma_z(x)\rangle$ nodes on opposite $\langle\sigma_x(x)\rangle$ axes, while each interval can accommodate only one $\langle\sigma_x(x)\rangle$ node; otherwise accommodation of more $\langle\sigma_x(x)\rangle$ nodes would totally outnumber the $2n$, $\langle\sigma_x(x)\rangle$ nodes due to the $\langle\sigma_z(x)\rangle$ reflection symmetry mentioned near (29).

In the above analysis, we have seen that the alternate nodes from the neighboring Hermite polynomials are driving the full spin winding. To get some more insight, in Appendix B we compare different combinations of the Fock basis which show that the superposition between the neighboring Fock states, $|n-1, \uparrow\rangle$ and $|n, \downarrow\rangle$ as in (7), leads to a nontrivial spin winding, while the other superpositions between non-neighboring bases tend to generate spin trajectory returns and cancel the spin winding. This analysis not only verifies the full winding behavior addressed above but also provides an understanding of the various spin-winding knots emerging in the $\lambda \neq 0$ case [31] in which non-neighboring bases are involved.

Summarizing the above analysis, we can rigorously conclude that the spin is in full winding without antiwinding nodes. The nodes are in the counterclockwise sequence 1234 as in Fig. 2(a) or the clockwise sequence 1432 on the (1) positive- $\langle\sigma_z(x)\rangle$ axis (closed circle), (2) positive- $\langle\sigma_x(x)\rangle$ axis (closed square), (3) negative- $\langle\sigma_z(x)\rangle$ axis (open circle), (4) negative- $\langle\sigma_x(x)\rangle$ axis (open square), periodically until completing the total spin winding at infinity. Such clarification of the full winding behavior is necessary for the explicit extraction of the winding number later on in Sec. IV F.

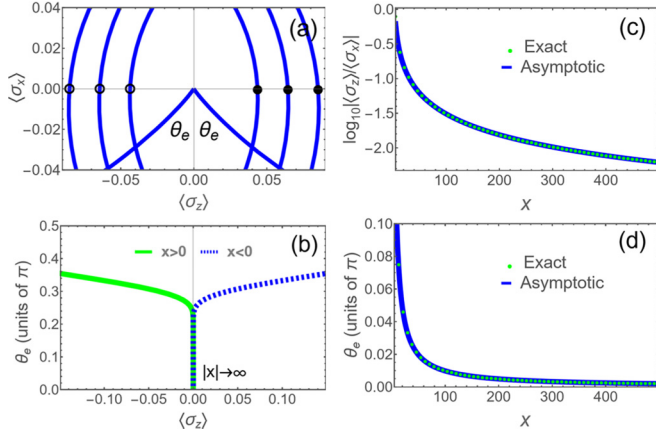


FIG. 3. Vanishing external spin-winding angle at infinity. (a) Close-up of the spin winding in Fig. 1(f) around the origin. Here θ_e is the external winding angle at large x . (b) Plot of θ_e versus $\langle\sigma_x(x)\rangle$ in the $|x| \rightarrow \infty$ limit. Also shown are plots of (c) $\log_{10}[\langle\sigma_z(x)\rangle/\langle\sigma_x(x)\rangle]$ and (d) θ_e versus large x by the exact solution (dots) and the asymptotic expression (35) (solid line).

E. Spurious fractional winding angle at infinity

Apart from the main part of the spin winding in the node sequence, the total winding angle is also partially determined by the winding at infinity. A plot focusing on the external winding angle θ_e is illustrated in Fig. 3(a). At first glance one might think that θ_e is fractionally finite. However, a more careful tracking of θ_e at larger $|x|$ reveals that θ_e is approaching zero at infinity, as shown in Fig. 3(b). Indeed, at infinity the leading term of Hermite polynomials is

$$H_n(x) \rightarrow (2x)^n, \quad (34)$$

so we have the ratio of the spin texture

$$\frac{\langle\sigma_z(x)\rangle}{\langle\sigma_x(x)\rangle} \rightarrow -\frac{\Omega_{n\omega\chi} + \eta\sqrt{4g^2n + \Omega_{n\omega\chi}^2}}{\sqrt{2}g} \frac{1}{x}, \quad (35)$$

which is approaching zero. As demonstrated in Fig. 3(c), this asymptotic behavior (solid line) agrees well with the exact ratio (dots) obtained by Eqs. (26) and (27). Correspondingly, as shown in Fig. 3(d), the external angle of spin winding is vanishing at infinity

$$\theta_\infty = \arctan \frac{\langle\sigma_z(x)\rangle}{\langle\sigma_x(x)\rangle} \rightarrow 0. \quad (36)$$

This vanishing external angle achieves an integer number of total spin-winding angles as formulated in the next section.

F. Winding number in terms of nodes

We can know the rounds of spin winding by the winding number around the origin in the $\langle\sigma_z\rangle$ - $\langle\sigma_x\rangle$ plane as calculated by

$$n_{zx} = \frac{1}{2\pi} \int_{-\infty}^{\infty} \frac{\langle\sigma_z(x)\rangle\partial_x\langle\sigma_x(x)\rangle - \langle\sigma_x(x)\rangle\partial_x\langle\sigma_z(x)\rangle}{\langle\sigma_z(x)\rangle^2 + \langle\sigma_x(x)\rangle^2} dx, \quad (37)$$

which has also been applied in topological classification in nanowire systems and quantum systems with geometric

driving [115–118]. With the normalized spin texture

$$\langle\bar{\sigma}_{z,x}(x)\rangle = \frac{\langle\sigma_{z,x}(x)\rangle}{\sqrt{\langle\sigma_z(x)\rangle^2 + \langle\sigma_x(x)\rangle^2}}, \quad (38)$$

we can rewrite the integrand as

$$\begin{aligned} & \frac{\langle\sigma_z(x)\rangle\partial_x\langle\sigma_x(x)\rangle - \langle\sigma_x(x)\rangle\partial_x\langle\sigma_z(x)\rangle}{\langle\sigma_z(x)\rangle^2 + \langle\sigma_x(x)\rangle^2} \\ &= \frac{-\partial_x\langle\bar{\sigma}_z(x)\rangle}{\eta_x\sqrt{1 - \langle\bar{\sigma}_z(x)\rangle^2}} = \frac{\partial_x\langle\bar{\sigma}_x(x)\rangle}{\eta_x\sqrt{1 - \langle\bar{\sigma}_x(x)\rangle^2}}, \end{aligned} \quad (39)$$

where $\eta_{x,z} = \text{sign}(\bar{\sigma}_{x,z}(x))$, so that the integral (37) can be worked out explicitly in terms of either $\langle\sigma_x(x)\rangle$ or $\langle\sigma_z(x)\rangle$ nodes

$$\begin{aligned} n_{zx} &= -\sum_{i=0}^{M_x} \frac{\arcsin\langle\bar{\sigma}_z(x_{Z,i+1})\rangle - \arcsin\langle\bar{\sigma}_z(x_{Z,i})\rangle}{2\pi\eta_x(i)} \quad (40) \\ &= \sum_{i=1}^{M_z} \frac{\arcsin\langle\bar{\sigma}_x(y_{Z,i+1})\rangle - \arcsin\langle\bar{\sigma}_x(y_{Z,i})\rangle}{2\pi\eta_z(i)}. \end{aligned} \quad (41)$$

Attention should be paid here that the summation in Eq. (40) [Eq. (41)] is over M_x , $\langle\sigma_x(x)\rangle$ nodes [M_z , $\langle\sigma_z(x)\rangle$ nodes], i.e., over $x_{Z,i}$ [$y_{Z,i}$], not over the nodes of the variable $\langle\sigma_z(x)\rangle$ [$\langle\sigma_x(x)\rangle$] in the integrand (39). Corresponding to $\eta_{x,z}$ in (39), $\eta_x(i)$ [$\eta_z(i)$] is the sign of $\langle\sigma_x(x)\rangle$ [$\langle\sigma_z(x)\rangle$] in space section $x \in (x_{Z,i}, x_{Z,i+1})$ [$x \in (y_{Z,i}, y_{Z,i+1})$], which can be represented by the sign of a $\langle\sigma_z(x)\rangle$ [$\langle\sigma_x(x)\rangle$] node in the section. The edge sections $i=0$, $M_{x,z}$ are $(-\infty, x_{Z,1})$ and (x_{Z,M_x}, ∞) [$(-\infty, y_{Z,1})$ and (y_{Z,M_z}, ∞)]. We have set $x_{Z,0} = -\infty$ and $x_{Z,M_x+1} = \infty$ ($y_{Z,0} = -\infty$ and $y_{Z,M_z+1} = \infty$).

Noting that $\arcsin\langle\bar{\sigma}_z(y_{Z,i})\rangle = \frac{\pi}{2} \text{sign}[\bar{\sigma}_z(y_{Z,i})]$ and $\arcsin\langle\bar{\sigma}_x(x_{Z,i})\rangle = \frac{\pi}{2} \text{sign}[\bar{\sigma}_x(x_{Z,i})]$, we arrive at

$$\begin{aligned} n_{zx} &= -\sum_{i=0}^{M_x} \frac{\text{sgn}\langle\bar{\sigma}_z(x_{Z,i+1})\rangle - \text{sgn}\langle\bar{\sigma}_z(x_{Z,i})\rangle}{4\eta_x(i)} \quad (42) \\ &= \sum_{i=0}^{M_z} \frac{\text{sgn}\langle\bar{\sigma}_x(y_{Z,i+1})\rangle - \text{sgn}\langle\bar{\sigma}_x(y_{Z,i})\rangle}{4\eta_z(i)}, \end{aligned} \quad (43)$$

where we have set the function $\text{sgn}(\bar{\sigma}_{x,z}) = \text{sign}(\bar{\sigma}_{x,z})$ for the nodes and $\text{sgn}(\bar{\sigma}_{x,z}) = 2 \arcsin(\bar{\sigma}_{x,z})/\pi$ for the infinity ends. Finally, only the neighboring nodes with opposite signs contribute.

The expressions (40)–(42) are valid for general spin windings. Note that the original version of the winding number (37) involves calculus of both the integral and differential, which is numerically more difficult to treat. In contrast, Eqs. (42) and (43) are simple algebraic expressions comprising only a finite number of nodes of $\langle\sigma_z(x)\rangle$ and $\langle\sigma_x(x)\rangle$, which greatly simplifies the calculation of the winding number. Moreover, the integral (37) depends on the topological structure of the spin texture geometrically. The equivalence of Eqs. (42) and (43) to Eq. (37) indicates that, given the few points of nodes, the topological winding number remains the same no matter how the spin texture is geometrically deformed, which reclaims the original sense of topological classification in the so-called rubber-sheet geometry. As Eqs. (42) and (43) are nodes whose order encodes the topological message by an algebraic code as at the end of

Sec. IV D, it is also a demonstration of bridging of the geometrical topology and the algebraic topology, here physically in the context of the wave function and spin winding.

According to the discussion in Secs. IV D and IV E, the spin is in full winding without antiwinding nodes and the external winding angle at infinity is vanishing. Note that there are $M_x = 2n$, $\langle\sigma_x(x)\rangle$ nodes and $M_z = 2n - 1$, $\langle\sigma_z(x)\rangle$ nodes, while the infinity ends only contribute to $\text{sgn}(\bar{\sigma}_z)$ to complete a full integer round of winding. Thus, from (40) and (41) we can readily conclude that the magnitude of the spin-winding number is

$$|n_w| = |n_{zx}| = n. \quad (44)$$

The sign of n_w is determined by the winding direction, which is reflected in $\eta_{x,z}(i)$ and can be more explicitly obtained by the status at infinity as in the following.

G. Winding direction

Since the winding is smooth without antiwinding nodes and the external winding angle is zero at infinity $\theta_\infty \rightarrow 0$, the winding direction can be determined by the signs of $\langle\sigma_z(x)\rangle$ and $\langle\sigma_x(x)\rangle$ at infinity where the spin winding starts and ends. The winding will be counterclockwise if $\langle\sigma_z(x)\rangle$ starts to grow negatively (positively) while $\langle\sigma_x(x)\rangle$ increases positively (negatively), which happens in the second (fourth) quadrant; otherwise the winding is clockwise if $\langle\sigma_z(x)\rangle$ and $\langle\sigma_x(x)\rangle$ start in the first (third) quadrant. Clockwise winding starting in the second (fourth) quadrant or counterclockwise winding starting in the first (third) quadrant is excluded as that would lead to $M_z = 2n + 1 > M_x = 2n$, which conflicts with the previously discussed node numbers determined by Eqs. (26) and (27). Thus, the winding is counterclockwise (clockwise) if the sign

$$s_w = \text{sign} \left. \frac{\langle\sigma_z(x)\rangle}{\langle\sigma_x(x)\rangle} \right|_{x \rightarrow -\infty} = \text{sign}(\Omega_{n\omega\chi} + \eta\sqrt{4g^2n + \Omega_{n\omega\chi}^2}) \quad (45)$$

is negative (positive). This indicates that all states with $\eta = -1$ have a counterclockwise spin-winding direction, while the winding direction of the states with $\eta = +1$ is opposite. The ground state is composed of $\eta = -1$ states and thus has a counterclockwise winding direction.

Thus, the energy branch label η and the excitation number n together give the complete information of the spin-winding number for state $\psi_n^{(x,\eta)}$,

$$n_w = -s_w n = -\eta n, \quad (46)$$

which is the topological quantum number. The minus sign in (46) is added to assign positive n_w to the counterclockwise winding direction. Now we see that both η and n are endowed with topological connotations, representing the winding direction and the magnitude of the winding number, respectively.

H. Topological phase diagram

For an overall view of all the phase transitions, we show the ground-state phase diagrams in the g - ω , χ - ω , and χ - g planes

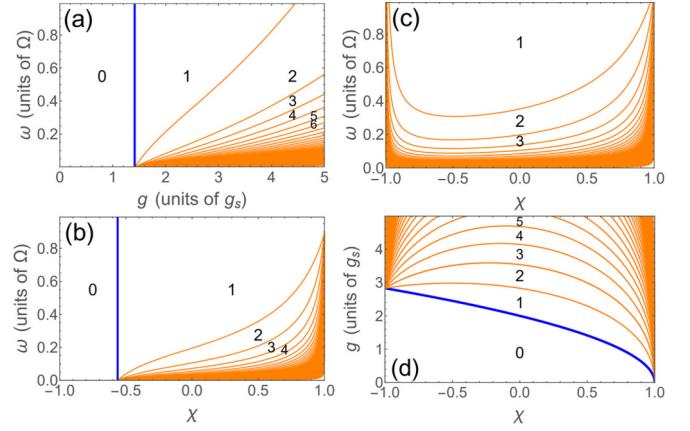


FIG. 4. Topological phase diagrams. The ground-state spin-winding number n_w is plotted in the (a) g - ω plane at $\chi = 0.5$, (b) χ - ω plane for $g = 2.5g_s$ at $\chi = 0.5$, (c) χ - ω plane for $g = 3.0g_s$ at $\chi = 0.5$, and (d) χ - g plane at $\omega = 0.3\Omega$.

in Fig. 4, where the numbers mark n_w . The phase boundaries shifting states from $\psi_n^{(x,-1)}$ to $\psi_{n+1}^{(x,-1)}$ can be analytically obtained for $n = 0$,

$$g_c^{(0,1)} = 2g_s\sqrt{1-\chi}, \quad (47)$$

and for $n > 0$,

$$g_c^{(n,n+1)} = 2g_s\sqrt{(\chi_+ + 2n\chi_+\chi_-)\tilde{\omega} - \chi + S_r}, \quad (48)$$

where $S_r = \sqrt{(1 - \chi_+\tilde{\omega})^2 + 4n(n+1)\chi_+\chi_-\tilde{\omega}^2}$, $\tilde{\omega} = \omega/\Omega$, $\chi_\pm = 1 \pm \chi$, and $g_s = \sqrt{\omega\Omega}/2$. In Fig. 4 the thick blue line represents the principal boundary $g_c^{(0,1)}$ where the first transition occurs from the $n_w = 0$ phase to the $n_w = 1$ phase when the coupling g is increasing at a fixed Stark coupling χ in Fig. 4(a) or when χ is increasing at a fixed g in Fig. 4(b). The principal boundary disappears if the fixed g is larger than $g_c^{(0,1)}$ as in Fig. 4(c), which can be seen more clearly in Fig. 4(d), where $g_c^{(0,1)}$ exists in a finite range within the physical regime $\chi \in [-1, 1]$. Here we find that the critical couplings can be tuned by χ .

V. SIMULTANEOUS OCCURRENCE OF LANDAU-CLASS AND TOPOLOGICAL-CLASS TRANSITIONS

As mentioned in the Introduction, the Landau-class transitions break the symmetry while the topological-class transitions preserve the symmetry. Conventionally, these two classes of transitions are incompatible due to the contrary symmetry requirements. However, here the principal transition at $g_c^{(0,1)}$ provides a paradigmatic case of exception, as it turns out to be both a Landau-class transition and a topological-class transition simultaneously.

A. Topological-class transition feature at $g_c^{(0,1)}$: Transition of spin-winding topology

As addressed in the preceding section, we have seen the topological nature of all the transitions, including the principal transition at $g_c^{(0,1)}$. To have direct insight into the topological transition for the principal transition, in Figs. 5(a) and 5(b) we plot spin profiles in the $\langle\sigma_z(x)\rangle$ - $\langle\sigma_x(x)\rangle$ plane for the phases

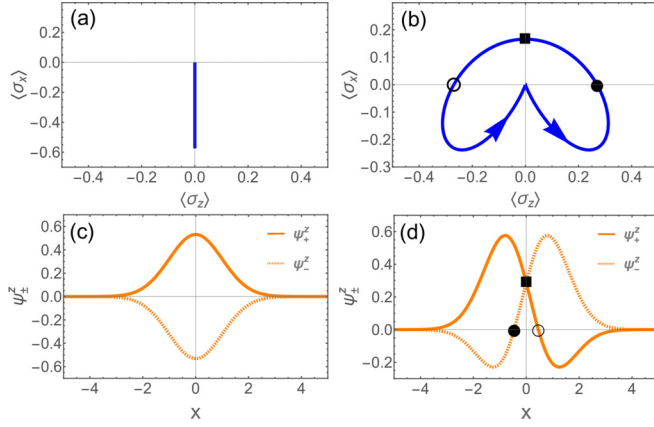


FIG. 5. Simultaneous occurrence of the symmetry-protected topological-class transition and the symmetry-breaking Landau-class transition. The ground-state spin profile is shown in the $\langle \sigma_z(x) \rangle - \langle \sigma_x(x) \rangle$ plane in the (a) $n_w = 0$ phase and (b) $n_w = 1$ phase. The ground-state wave function $\psi_{\pm}^z(x)$ is shown with (c) \hat{P}_x and \hat{P}_σ symmetries in the $n_w = 0$ phase and (d) broken \hat{P}_x and \hat{P}_σ symmetries in the $n_w = 1$ phase. Here (a) and (c) $g = 0.8g_s$ and (b) and (d) $g = 2.0g_s$ at $\omega = 0.6\Omega$ and $\chi = 0.5$.

before and after the transition. As we can see, in the $n_w = 0$ phase the spin profile is completely flat [$\langle \sigma_z(x) \rangle = 0 \forall x$] and does not wind at all as in Fig. 5(a), while in the $n_w = 1$ phase the spin is winding nontrivially as in Fig. 5(b). These two totally different spin-winding styles provide a sharp topological contrast for recognition of the topological nature of the transition.

B. Landau-class transition feature at $g_c^{(0,1)}$: Symmetry breaking of space inversion and spin reversion

The $n_w = 0$ phase before the principal transition at $g_c^{(0,1)}$ is also special as it possesses more symmetries than the Hamiltonian. Indeed, besides the parity symmetry, the state $\psi_0 = |0, \downarrow\rangle$ in this phase has symmetries of space inversion and spin reversion

$$\hat{P}_x \psi_0 = \psi_0, \quad \hat{P}_\sigma \psi_0 = -\psi_0, \quad (49)$$

where

$$\hat{P}_x = (-1)^{a^\dagger a}, \quad \hat{P}_\sigma = \sigma_x. \quad (50)$$

In the position space on the σ_z basis the wave function takes the form $\psi_0 = \psi_{0,+}^z(x)|\uparrow\rangle + \psi_{0,-}^z(x)|\downarrow\rangle = [\phi_0(x)|\uparrow\rangle - \phi_0(x)|\downarrow\rangle]/\sqrt{2}$, where $\phi_0(x)$ is the Gaussian function. The symmetry operator \hat{P}_x actually inverts the space [27] of a function $\hat{P}_x F(x) = F(-x)$, which gives

$$\hat{P}_x \psi_0(x) = \psi_0(x), \quad (51)$$

$$\hat{P}_\sigma \psi_0(x) = -\psi_0(x), \quad (52)$$

as $\phi_0(x)$ is an even function. The space inversion and spin reversion are more directly visible from the plot of the wave-function components in Fig. 5(c). It should be mentioned that these symmetries in Eqs. (17)–(20) are rigorously fulfilled at any finite frequency, in contrast to the QRM and the anisotropic QRM where the low-frequency condition is

required for the validity of these symmetries [28]. The unlimited frequency condition greatly relaxes the experimental requirements for QPTs [21].

On the contrary, in other phases with $n_w \neq 0$, the symmetries of space inversion and spin reversion are broken. Indeed, from Eqs. (17)–(20) we can easily recognize

$$\hat{P}_x \psi_n^{(z,\eta)}(x) \neq \pm \psi_n^{(z,\eta)}(x), \quad (53)$$

$$\hat{P}_\sigma \psi_n^{(z,\eta)}(x) \neq \pm \psi_n^{(z,\eta)}(x), \quad (54)$$

in contrast to the symmetry-preserving Eqs. (51) and (52). In Fig. 5(d) with $n_w = 1$ we see directly that the wave function is asymmetric under either space inversion or spin reversion.

Thus, the principal transition from state ψ_0 to state $\psi_1^{(z,\eta)}$ is accompanied by the symmetry breaking of both space inversion and spin reversion. This symmetry-breaking feature holds without approximation at any frequency. In such a symmetry-breaking sense, the principal transition also belongs to the Landau class of transitions. Also, in the Landau theory the energy is expressed as a functional of some order parameters. We discuss the variational energy as a functional of the order parameters in symmetry breaking around the transition in Appendix C.

C. Key for reconciliation of the two contrary transition classes: Unbroken higher symmetry

We have seen at $g_c^{(0,1)}$ the simultaneous occurrence of the topological class of transition and the Landau class of transition, which are conventionally incompatible due to opposite symmetry requirements. The key for their simultaneous occurrence or coexistence essentially lies in the reconcilable situation that the symmetry which the topological class of transition preserves is actually different from the symmetries which the Landau class of transition breaks. Indeed, the symmetry that protects the topological feature of the spin winding for the eigenstates in the transitions is the parity symmetry \hat{P} , which comprises both the space inversion and the spin reversal

$$\hat{P} = \hat{P}_x \hat{P}_\sigma. \quad (55)$$

As mentioned in Sec. II, the g_y term in the coupling is effectively the Rashba spin-orbit coupling or equal-weight mixture of the linear Dresselhaus and Rashba spin-orbit couplings [28–31], which involves the spin nontrivially and drives the spin winding. The parity symmetry guarantees the symmetric spin texture in (29) and its connection at the two infinity ends in the position variation, which establishes the symmetry situation for the TPTs. Note that both before and after the transition $g_c^{(0,1)}$ this parity symmetry that actually protects all the TPTs is still preserved

$$\hat{P} \psi_0(x) = -\psi_0(x), \quad (56)$$

$$\hat{P} \psi_n^{(z,\eta)}(x) = \pm \psi_n^{(z,\eta)}(x), \quad (57)$$

even when the subsymmetries in both the space inversion and the spin reversal are broken. Therefore, the conventionally opposite symmetry requirements for the Landau class and topological class of phase transitions reconcile each other here and we see the simultaneous occurrence or coexistence of the two contrary transition classes.

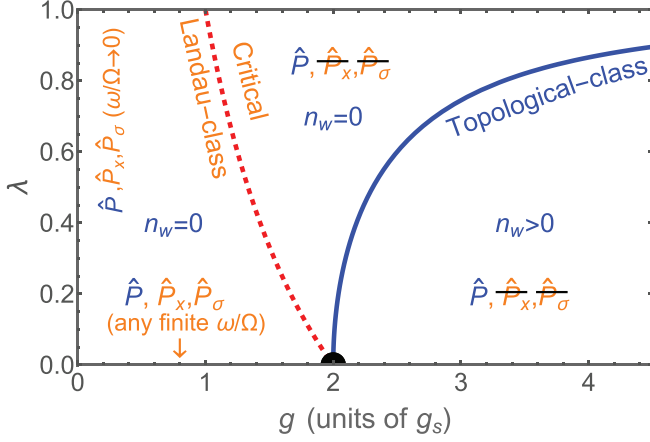


FIG. 6. Parameter tuning for symmetries and simultaneous occurrence of topological-class and Landau-class transitions. The topological-class transition (blue solid line) is protected by the parity symmetry \hat{P} , while the Landau-class transition (red dashed line) breaks the symmetries of \hat{P}_x and \hat{P}_σ (the strikethroughs mark the symmetry breaking). The black dot at $\lambda = 0$ indicates the simultaneous transition occurrence.

D. Parameter tuning for symmetries and simultaneous occurrence of topological-class and Landau-class transitions

It might be helpful to provide an overview of the evolutions and simultaneous occurrence of the two classes of transitions in tuning the system parameters. Figure 6 shows the evolutions of the principal topological transition boundary (blue solid line) and the Landau-class transition boundary (red dashed line) with the variation of the anisotropy rate λ at a fixed Stark coupling ratio χ (illustrated by $\chi = 0$). Under a finite anisotropy, the Landau-class transition occurs in the low-frequency limit $\omega/\Omega \rightarrow 0$, which validates the symmetries \hat{P}_x and \hat{P}_σ before the transition [28]. These symmetries are broken after the transition, as indicated by the strikethroughs in the figure. This Landau-class transition does not change the spin-winding number, as $n_w = 0$ both before and after the transition. Here, at finite λ the Landau-class transition is of second order and the order parameters manifest critical universality for both the anisotropy [25,28,30] and the Stark nonlinear coupling [30]. After the topological transition the spin-winding number becomes finite ($n_w > 0$); it is protected by the parity symmetry \hat{P} , which holds in all regions. Both boundaries can be analytically extracted [30]:

$$g_{\text{Landau}}^{\lambda,\chi} = \frac{2\sqrt{(1-\chi)}}{1+|\lambda|} g_s, \quad (58)$$

$$g_{\text{topo}}^{\lambda,\chi} = \frac{2\sqrt{1-\chi^2}}{\sqrt{(1+\chi) - \lambda^2(1-\chi)}} g_s. \quad (59)$$

Note that $g_{\text{Landau}}^{\lambda,\chi}$ and $g_{\text{topo}}^{\lambda,\chi}$ are apart from each other at finite λ , as we see in Fig. 6. These two boundaries meet at $\lambda = 0$, as marked by the black dot in the figure, to realize the simultaneous occurrence at

$$g_{\text{simul}} = 2g_s\sqrt{1-\chi} = g_c^{(0,1)}. \quad (60)$$

We recall here at $\lambda = 0$ that, as mentioned below Eqs. (51) and (52), the symmetries \hat{P}_x and \hat{P}_σ hold for all finite frequencies, without the constraint of a low-frequency limit as in the finite- λ regime. Now at the simultaneous occurrence, the Landau-class transition becomes first order, as addressed in Appendix C.

Although Fig. 6 is illustrated for $\chi = 0$, we can have the simultaneous occurrence in the entire physical regime of χ . We can tune the coupling value of simultaneous occurrence by χ as the blue (thick) line in Fig. 4(d).

VI. UNDERSTANDING UNCONVENTIONAL TOPOLOGICAL TRANSITIONS IN THE PRESENCE OF A COUNTERROTATING TERM

Most TPTs in the anisotropic QRM are conventional ones [28] that occur with gap closing, like those in condensed matter [93,104–109]. Unconventional TPTs without gap closing also exist [29,30] analogously to the unconventional cases in the quantum spin Hall effect with strong electron-electron interactions [110] and the quantum anomalous Hall effect with disorder [111]. These unconventional TPTs lie in the ground state by a mechanism of node introduction from infinity [29,30]. On the other hand, it is found that unconventional TPTs emerge more frequently in excited states, especially around level anticrossings [31]. We give an example of phase diagrams with unconventional TPTs in Appendix D. Here we can gain some insight from the JC-Stark model into the origin of such unconventional TPTs in excited states.

Figure 7(a) shows the energy spectrum of the JC-Stark model, where levels are crossing among all the states with negative parity (blue solid line) and positive parity (red dotted line). Figure 7(b) gives the spin-winding number n_w (solid line) of the ground state ($j_E = 1$) which jumps always at parity variation (dotted line) and gap closing [similar to the solid line in Fig. 7(f)]. The spin winding can change direction in excited states, as indicated by the negative values of n_w in Fig. 7(d) for the state $j_E = 20$ according to the discussion in Sec. IV G. Each jump of n_w is accompanied by a TPT. In particular, some TPTs occur without parity variation, as illustrated in Fig. 7(e) for the state $j_E = 2$, which comes from the level crossing between same-parity states. Note here that the gap is still closing at the transitions despite no parity variation. What is interesting is that once we add anisotropy, e.g., $\lambda = 0.01$, the gap at these TPTs opens, as demonstrated by the energy spectrum in Fig. 7(b) and more clearly by the dotted line in Fig. 7(f). This gap opening accounts for the aforementioned unconventional TPTs in the excited state.

A clearer explanation can be given by regarding the counterrotating term as a perturbation around these transitions, which mainly involves the two level-crossing states $\psi_n^{(x,\eta)}$ and $\psi_{n'}^{(x,\eta')}$ with energies $\varepsilon_1 = E^{(n,\eta)}$ and $\varepsilon_2 = E^{(n',\eta')}$ and winding numbers $n_{w,1} = -\eta n$ and $n_{w,2} = -\eta' n'$. On the basis of these two states, the Hamiltonian in matrix form can be written as

$$H \approx \begin{pmatrix} E^{(n,\eta)} & d \\ d & E^{(n',\eta')} \end{pmatrix}, \quad (61)$$

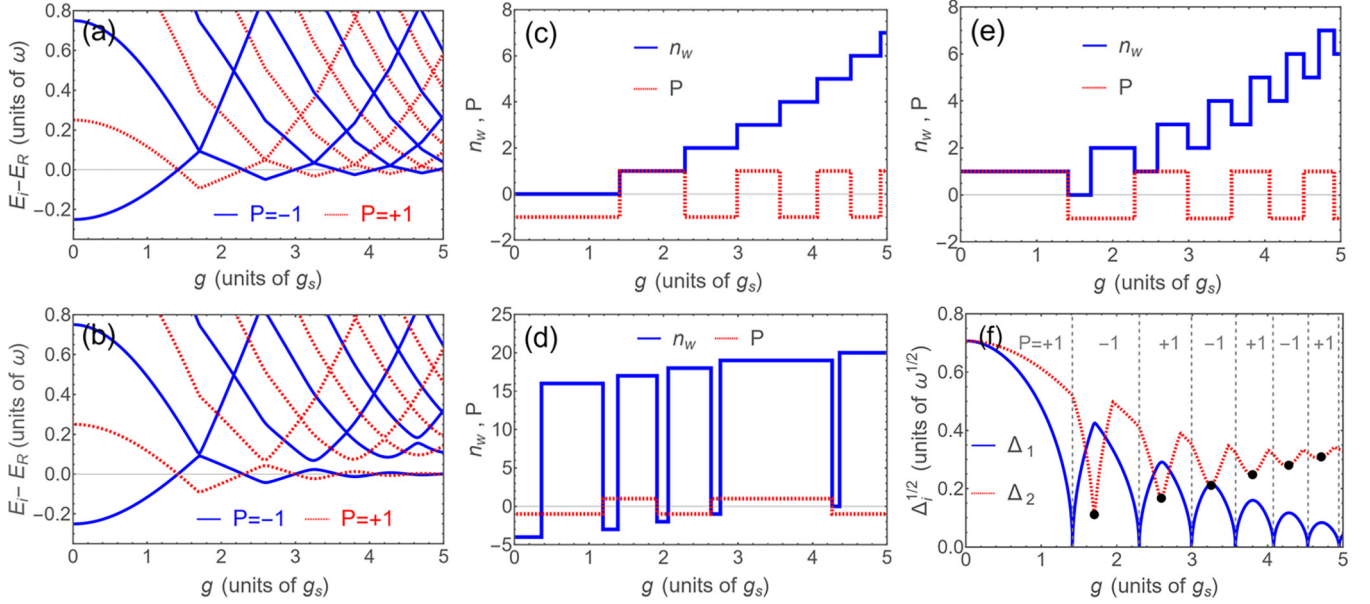


FIG. 7. Topological transitions without parity variation and origin for unconventional topological transitions without gap closing. The energy spectrum $E_i - E_R$ is shown (a) in the absence ($\lambda = 0$) and (b) in the presence ($\lambda = 0.01$) of the counterrotating term, with the reference energy $E_R = (E_2 + E_1)/2$. The spin-winding number n_w (blue solid line) and parity P (red dotted line) are plotted for (c) $j_E = 1$, (d) $j_E = 20$, and (e) $j_E = 2$ at $\lambda = 0$. (f) First and second excitation gaps $\Delta_i = E_{i+1} - E_i$ at $\lambda = 0.01$. The dots in (f) are results from Eq. (63). Here $\omega = 0.3\Omega$ and $\chi = 0.5$ in all panels.

where

$$d = \langle \psi_n | H_\lambda | \psi_{n'} \rangle = \lambda g \sqrt{n' + 1} \frac{C_{n\uparrow}^{(\eta)} C_{n'\downarrow}^{(\eta')}}{\sqrt{N_n N_{n'}}} \delta_{n, n'+2} + \lambda g \sqrt{n' - 1} \frac{C_{n\downarrow}^{(\eta)} C_{n'\uparrow}^{(\eta')}}{\sqrt{N_n N_{n'}}} \delta_{n, n'-2} \quad (62)$$

and H_λ is the counterrotating term in (3) beyond the JC-Stark model. The crossing levels are split as $E_\pm = \frac{1}{2}(E^{(n, \eta)} + E^{(n', \eta')}) \pm \Delta$ with a gap opening at the level-crossing point $E^{(n, \eta)} = E^{(n', \eta')}$,

$$\Delta = \sqrt{(E^{(n, \eta)} - E^{(n', \eta')})^2 + 4d^2} \rightarrow 2|d|, \quad (63)$$

which is finite for $n = n' \pm 2$, leading to the level anticrossing. The validity of Eq. (63) is confirmed by the dots, which match well the numerical result by exact diagonalization [27,31] shown by the dotted line in Fig. 7(f). A comparison of Eq. (63) with the exact diagonalization in varying λ is presented in Appendix E.

From Eqs. (62) and (63) we see that the gap opening does not occur for crossing states with different parity, since they have even and odd n , respectively, as indicated by $P = (-1)^n$ from Eq. (9). Note that the small λ here is a perturbation which is not yet enough to change the winding numbers so that n_w remains similar to the $\lambda = 0$ case in Fig. 7(e). Thus, the TPTs originally at level crossing now become unconventional TPTs without gap closing as the gap is opening. Larger λ may induce more unconventional TPTs than those inherited from the $\lambda = 0$ case at the gap opening [31]. Finally it should be noted that such unconventional TPTs are still protected by the parity symmetry as the added term H_λ preserves the parity symmetry $[H_\lambda, \hat{P}] = 0$. The above analysis provides a simple

but clear understanding of the unconventional TPTs in excited states.

At larger λ an explicit analytic formulation is not available as the perturbation treatment becomes invalid; one may need to fall back on the numerical method of exact diagonalization [27,31] as illustrated in Appendix D. Still, one could argue by some adiabatic [101,117] continuity, despite that a more strict analysis may need some further work. In fact, the TPTs emerge when one goes from the low-frequency limit to finite frequencies [28,30], while at finite frequencies the adiabatic approximation [126] becomes more valid [58]. On the other hand, as mentioned in Sec. II, the g_y terms in (6) resemble [30] the Rashba spin-orbit coupling in nanowires [114–118]. Here the gap opening occurs at large couplings which lead to large effective Rashba couplings, while we know from nanowires that a strong Rashba coupling lies in an adiabatic regime for the geometric phase which is connected to the spin winding [115]. Indeed, although the wave function may be continuously deformed, the topological feature remains similar in anisotropy variation within a topological phase as demonstrated [28–31] by the polaron picture [21,27,29,60,101]. In such adiabatic-favorable situations, one may speculate that the main feature of the conventional and unconventional TPTs may be extended to a larger λ regime, which really is the case, as illustrated in Fig. 10 in Appendix D.

VII. CONCLUSION

We have presented a rigorous study to show the topological nature of transitions in the Jaynes-Cummings model generally with Stark nonlinear coupling, which is a fundamental model for light-matter interactions. The exact and explicit solution of the model enabled us to analytically analyze the

nodes of the eigenfunctions and establish the exact correspondence to the nodes in the spin texture. In light of the Hermite polynomial properties, we have proven that the spin nodes on $\langle\sigma_z(x)\rangle$ and $\langle\sigma_x(x)\rangle$ axes are interlacing on positive and negative axes, and thus the node sequence forms a smooth spin winding without antiwinding nodes. At this point we found it is the superposition between the neighboring Fock states, as induced by the rotating-wave terms in the $\lambda = 0$ case, that plays a crucial role in generating the non-trivial spin winding, while the other superpositions between non-neighboring bases lead to spin trajectory returns and cancel the spin winding. This finding not only verifies the smooth winding behavior in the JC-Stark model here but also provides an understanding of the various spin-winding knots emerging in the $\lambda \neq 0$ case [31], in which non-neighboring bases are involved. In particular, the spurious fractional winding angle at infinity was found to be an integer, which achieves a full winding. Thus, the phase transitions in the model have the nature of TPTs.

In the analysis we saw that the topological features are protected by the parity symmetry, which leads to symmetric and antisymmetric properties of $\langle\sigma_x(x)\rangle$ and $\langle\sigma_z(x)\rangle$ for a close form of spin windings. Note that the parity symmetry is present in most of the relevant coupled light-matter models, which accounts for the numeric finding of the ubiquity of TPTs in different light-matter interactions including anisotropy [28,29,31] and the Stark nonlinear coupling [30].

Based on a strict derivation, we reformulated the spin-winding number to facilitate the extraction of winding numbers by replacing the integral formula with an algebraic formula in terms of finite points of nodes, which also bridges the geometrical topology and the algebraic topology in a physical way. The excitation number and the energy branch label of eigenstates turn out to be the magnitude and the sign (winding direction) of the winding number; thus both are endowed with a topological connotation.

In particular, we have found that the $\langle\sigma_z(x)\rangle$ nodes are invariant, which might have potential advantage in designing topological devices as they provide robust topological information unaffected by variations of the parameters. The invariant nodes can also greatly reduce the experimental cost and simplify the identification of the topological states in experimental simulations.

We have also demonstrated that the principal transition has the character of the Landau class of phase transition besides that of the TPT, by pointing out the symmetry-breaking aspect and variational energy analysis as functionals of order parameters. Note that conventional Landau-class phase transitions and topological-class phase transitions are incompatible due to the contrary symmetry requirements. Here the principal transition established a paradigmatic case that a transition can simultaneously be both a symmetry-breaking Landau-class transition and a symmetry-protected topological-class transition. The key for the reconciliation of the two contradictory classes of transitions lies in the preserved higher symmetry which protects the TPTs despite the subsymmetries being broken in the Landau-class transition.

Moreover, we have applied our result to analyze the gap opening at some particular TPTs without parity variations in the presence of the counterrotating term, which gives an

analytical explanation for the unconventional TPTs without gap closing. Note that a gapped situation can avoid the detrimental time divergent problem in preparing the sensing state [54]; the unconventional TPTs may similarly have potential advantages in possible applications or designing quantum topological devices. In such a favorable situation, our understanding might be helpful for further exploring and exploiting unconventional TPTs in light-matter interactions.

Finally, it is worth mentioning that the model considered in the present work may be implemented in realistic systems, e.g., in superconducting circuits. Indeed, both the anisotropy [12,45,127–129] and the Stark nonlinear coupling [84–86] are adjustable. Besides realizations of ultrastrong couplings in the $\lambda \neq 0$ case [5,7,8,11–19], access to ultrastrong couplings are also possible for $\lambda = 0$ [130–132]. The position x can be represented by the flux of Josephson junctions and the spin texture might be measured by interference devices and a magnetometer [133]. One could also extract the wave function from the spin density, with the amplitude equal to the density square root and the sign determined by the cusp situation at the nodes (see Appendix F). In this sense the wave function also becomes an observable, while the full spin texture is directly available by Eqs. (21) and (22) in terms of the extracted wave function. The topological feature addressed in this work was found to be robust against non-Hermiticity induced by the dissipation and decay rates in practical systems [134]. These systems may provide platforms for possible tests or applications of our results. Our analysis might be relevant also for some other systems as the effective Rashba or Dresselhaus spin-orbit coupling in our model is similar to those in nanowires [114–118], cold atoms [119,135], and relativistic systems [136].

ACKNOWLEDGMENT

This work was supported by the National Natural Science Foundation of China through Grants No. 11974151 and No. 12247101.

APPENDIX A: BRIEF COMPARISON OF TOPOLOGICAL-CLASS AND LANDAU-CLASS PHASE TRANSITIONS

A TPT refers to the change of the topological structure in some physical space as a certain system parameter crosses a critical threshold. As a more definite definition, for the state function $\psi(u)$ possessing a topological structure, if there is a critical parameter u_c such that for any δu sufficiently small the topological structure of the state function $\psi(u)$ is different from that of $\psi(u + \delta u)$, then one can say that the system undergoes a TPT at u_c [137]. Here the state function is essentially the wave function, while the topological feature can also manifest in the physical properties. In our systems of light-matter interactions, we not only see the topological feature both in the wave function and in the physical properties (spin winding) but also show their correspondence as in Sec. IV B. The critical thresholds for the TPTs are given in Fig. 4.

Unlike the local order parameter in the Landau-class transition (LCT) [88], the topological structure is a global feature

TABLE I. Comparison of topological-class and Landau-class phase transitions.

Parameter	Landau class	Topological class
symmetry	broken	preserved
characterization	order parameter	topological number
property type	local	global
character variation	varying	invariant
gap situation	closing	closing (conventional) gapped (unconventional)

and finally represented by some topological quantum number. The topological number is invariant in a topological phase, in contrast to the Landau order parameter, which is varying with the system parameter even in the same phase. Nevertheless, the universality of the LCT may lie in the critical exponent γ for second-order transition, around which the order parameter varies with a form proportional to $|u - u_c|^\gamma$ [24,25,28,30,95]. Generally speaking, the LCT has a gap closing of the excitation energy of quantum type at zero temperature or of the free-energy or thermodynamical potential of classical type at finite temperature. Usually TPTs are concerned with the ground state [94], while topological classification can be extended also to the excited states [31]. For TPTs, gap closing is a necessary condition conventionally, while there are also unconventional TPTs in special cases in both condensed-matter [110,111] and light-matter interactions [29–31] that occur without gap closing. We give a brief comparison of these two essentially different phase transitions in Table I. The TPTs [28–31] and the LCTs [20–32] in light-matter interactions fit all these key features [28–31].

APPENDIX B: FOCK BASIS $(n-1)$ - n COMBINATION CRUCIAL FOR SPIN WINDING

In this Appendix we show that an $(n-1)$ - n combination for the Fock basis, as in the solution (7), is crucial for the full spin winding addressed in Sec. IV D. To see the difference of the basis combination, we consider a trial state with a more general n_1 - n_2 combination of the Fock basis

$$\psi_{\text{trial}}^{(x)} = (C_{n_1\uparrow}|n_1, \uparrow\rangle + C_{n_2\downarrow}|n_2, \downarrow\rangle), \quad (\text{B1})$$

up to a normalization factor. Here we assume real coefficients $C_{n_1\uparrow}$ and $C_{n_2\downarrow}$ as in (7) due to the fact that the eigenstates are

nondegenerate except at some level-crossing points. The spin texture for $\psi_{\text{trial}}^{(x)}$ can be obtained as

$$\langle\sigma_z(x)\rangle = \frac{2e^{-x^2}C_{n_1\uparrow}C_{n_2\downarrow}H_{n_1}(x)H_{n_2}(x)}{(C_{n_1\uparrow}^2 + C_{n_2\downarrow}^2)\sqrt{\pi 2^{n_1}2^{n_2}n_1!n_2!}}, \quad (\text{B2})$$

$$\langle\sigma_x(x)\rangle = \frac{e^{-x^2}[C_{n_1\uparrow}^x H_{n_1}(x)^2 - C_{n_2\downarrow}^x H_{n_2}(x)^2]}{(C_{n_1\uparrow}^2 + C_{n_2\downarrow}^2)\sqrt{\pi n_1!n_2!}}, \quad (\text{B3})$$

$$\langle\sigma_y(x)\rangle = 0, \quad (\text{B4})$$

where $C_{n_1}^x = 2^{-n_1}C_{n_1\uparrow}^2n_2!$ and $C_{n_2}^x = 2^{-n_2}C_{n_2\downarrow}^2n_1!$

For $n_1 = n_2$ it is obvious to see that $\langle\sigma_x(x)\rangle$ is proportional to $\langle\sigma_z(x)\rangle$ while sharing the same $H_{n_1}(x)^2$ polynomial factors; there is no spin winding, as illustrated by Fig. 8(a), where the spin winding is completely suppressed. For $n_1 = n_2 + 1$, this basis combination has alternate nodes of the Hermite polynomials, as in Fig. 1(d), that drives the spin in full winding as demonstrated in Sec. IV D, which is confirmed by Fig. 8(b). For $n_1 = n_2 + 2$, both $\langle\sigma_z(x)\rangle$ and $\langle\sigma_x(x)\rangle$ become symmetric,

$$\langle\sigma_z(-x)\rangle = \langle\sigma_z(x)\rangle, \quad \langle\sigma_x(-x)\rangle = \langle\sigma_x(x)\rangle, \quad (\text{B5})$$

due to $H_n(-x) = (-1)^n H_n(x)$. As a consequence, besides the broken reflection symmetry around the $\langle\sigma_x(x)\rangle$ axis, the spin winding in the $x > 0$ path will completely return to the $x < 0$ path, as indicated by the returning arrows in Fig. 8(c), which cancels the spin winding with a finally vanishing winding number. For $n_1 = n_2 + 3$, the reflection symmetry recovers; however, the alternate node order as in the $n_1 = n_2 + 1$ case is broken. The spin winding forms returning knots as in Fig. 8(d), which also cancel the total winding, thus yielding a vanishing spin-winding number as well.

These examples indicate that the $(n-1)$ - n basis combination coming from the rotating-wave term plays a crucial role in driving the spin winding. This simple analysis not only verifies the full winding behavior of the JC-Stark model in this work but also provides an understanding of the various spin-winding knots (returning loops) emerging in the $\lambda \neq 0$ case [31] in which all non-neighboring bases are involved [31] in an eigenstate with some weight distribution [27].

APPENDIX C: VARIATIONAL ENERGY AS A FUNCTIONAL OF ORDER PARAMETERS

In this Appendix we discuss the energy functional of order parameters in the situation of the symmetry breaking at the principal transition. Although the exact solution has been obtained in Sec. III, a reformulation of the energy as a functional of order parameters is more connected with the Landau theory

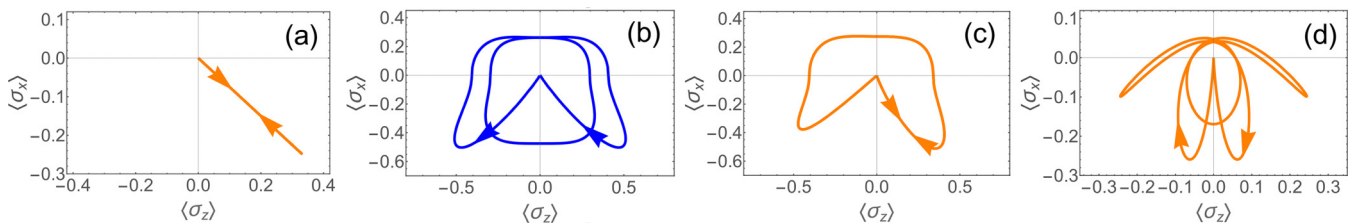


FIG. 8. Fock basis $(n-1)$ - n combination crucial for effective spin winding. Spin winding for the n_1 - n_2 Fock basis is shown for (a) $n_2 = n_1$, (b) $n_2 = n_1 + 1$, (c) $n_2 = n_1 + 2$, and (d) $n_2 = n_1 + 3$. Here $n_1 = 2$, $C_{n_2,\downarrow} = 1$, and $C_{n_1,\uparrow} = 0.5$. In (b) the spin-winding number is finite, while in the other cases the spin winding cancels itself.

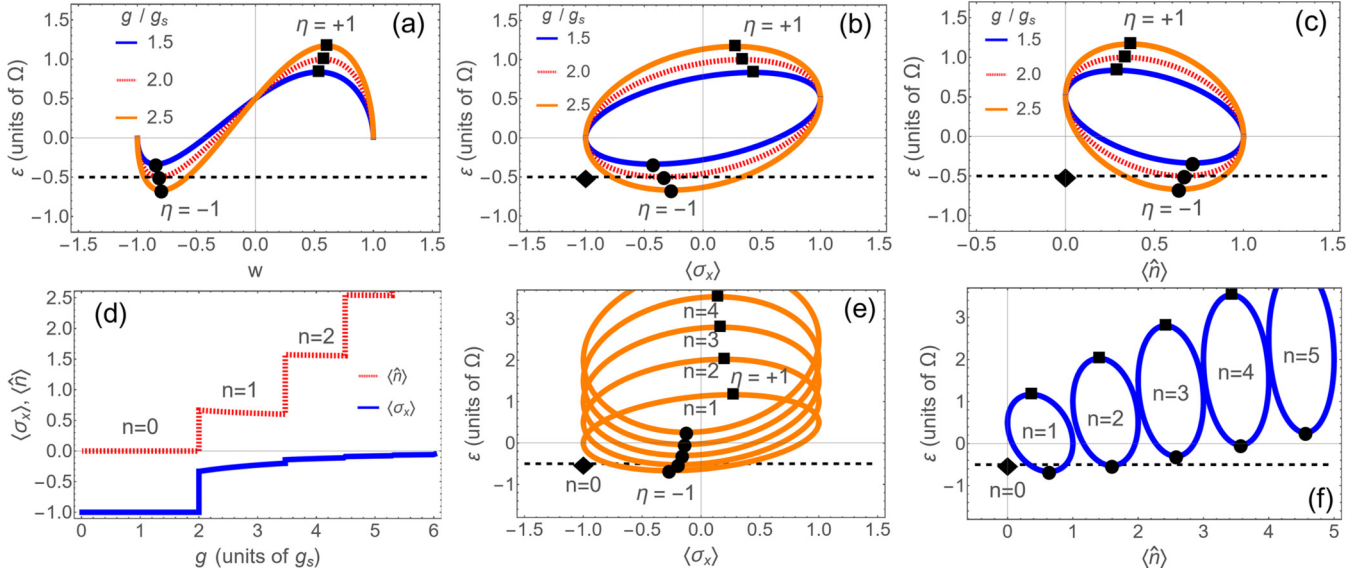


FIG. 9. Variational energy ε as a functional of order parameters in symmetry breaking: ε as a functional of (a) w , (b) $\langle\sigma_x\rangle$, and (c) $\langle\hat{n}\rangle$, for state ψ_1 before [$g = 1.5g_s$, orange (light) solid line], at ($g = 2.0g_s$, dotted line), and after [$g = 2.5g_s$, blue solid (dark) line] the transition $g_c^{(0,1)}$ in competition with the energy of state ψ_0 (thin dashed line); (d) $\langle\sigma_x\rangle$ (solid line) and $\langle\hat{n}\rangle$ (dotted line) versus g for the ground state; and ε as a function of (e) $\langle\sigma_x\rangle$ and (f) $\langle\hat{n}\rangle$ for states ψ_n at $g = 2.5g_s$. The circles mark the minimized energy and the squares label the maximized energy, which reproduces the exact JC energy in $\eta = -1$ and $+1$ branches, while the diamond locates the order parameters for ψ_0 . State ψ_0 (diamond) preserves the subsymmetries \hat{P}_x and \hat{P}_σ as indicated by integer numbers of $\langle\sigma_x\rangle$ and $\langle\hat{n}\rangle$, while the other states (circles and squares) break the subsymmetries as reflected by deviations of $\langle\sigma_x\rangle$ from ± 1 and $\langle\hat{n}\rangle$ from integer numbers. Here $\omega = 0.5\Omega$, $\lambda = 0$, and $\chi = 0$ in all panels.

of phase transitions. Under the constraint of the U(1) symmetry, the eigenstate of the JC-Stark model should be either a linear combination of bases $|n-1, \uparrow\rangle$ and $|n, \downarrow\rangle$,

$$\psi_n = \sqrt{1-w^2}|n-1, \uparrow\rangle + w|n, \downarrow\rangle, \quad (C1)$$

or composed solely of $\psi_0 = |0, \downarrow\rangle$. The energy of ψ_0 is simply $E^0 = -\Omega/2$, while the energy of ψ_n is variational with respect to the basis weight w ,

$$\varepsilon = \varepsilon_0 + [\omega - \Omega - \chi\omega(2n-1)]w^2 + 2\sqrt{ng}\sqrt{1-w^2}w, \quad (C2)$$

where $\varepsilon_0 = (1+\chi)\omega(n-1) + \frac{\Omega}{2}$ is independent of w . The minimization and maximization of ε with respect to w lead to

$$w_{\pm} = \pm \sqrt{\frac{4g^2n + A_w^2 \pm A_w\sqrt{4g^2n + A_w^2}}{8g^2n + 2A_w^2}}, \quad (C3)$$

where $A_w = [(2n-1)\chi - 1]\omega + \Omega$, which is equivalent [138] to (10) and (11) with $\eta = \pm$.

Note the relations

$$\langle\hat{n}\rangle = n - 1 + w^2, \quad (C4)$$

$$\langle\sigma_x\rangle = (1 - 2w^2). \quad (C5)$$

The variational energy can be rewritten in a functional form of the order parameter $\langle\sigma_x\rangle$ or $\langle\hat{n}\rangle$,

$$\varepsilon = \varepsilon_0 - C_\varepsilon(1 - \langle\sigma_x\rangle) + \eta\sqrt{ng}\sqrt{1 - \langle\sigma_x\rangle^2}, \quad (C6)$$

$$\varepsilon = \varepsilon_0 - 2C_\varepsilon(\langle\hat{n}\rangle + 1 - n) + \eta 2\sqrt{ng}\sqrt{(n - \langle\hat{n}\rangle)(\langle\hat{n}\rangle + 1 - n)}, \quad (C7)$$

where $C_\varepsilon = [\frac{\Omega-\omega}{2} + (n-\frac{1}{2})\chi\omega]$. Figure 9 illustrates some examples of the variational energy around the transition at $g_c^{(0,1)}$ in competition with the energy of ψ_0 . The circles mark the minimized energy, while the squares label the maximized energy. We see that when g is increasing, the minimized energy becomes lower than that of state ψ_0 , which triggers a first-order transition unlike the second-order transition in the QRM or the anisotropic QRM [27,30] in the low-frequency limit. The upper branch ($\eta = +1$) and the lower branch ($\eta = -1$) of the variational energy ε are connected and form energy circles as shown in Fig. 9(d). The lowest and highest points are the final energies, which together with E^0 reproduce the exact energies in Eq. (12) not only for the ground state but also for the excited states as demonstrated in Figs. 9(e) and 9(f).

Note that the energy and the order parameters of ψ_0 are represented by the diamonds in Figs. 9(b)–9(e), where the expectation value $\langle\sigma_x\rangle = \langle\hat{P}_x\rangle = -1$ implies the spin reversal symmetry in (51) and $\langle\hat{n}\rangle = 0$ indicates the space inversion symmetry in (52). As a contrast, the values of $\langle\sigma_x\rangle$ and $\langle\hat{n}\rangle$ for the minimum and maximum points on the energy circles deviate from the integer numbers, which means breaking of these symmetries.

APPENDIX D: PHASE DIAGRAMS IN THE g - λ PLANE AND EMERGING UNCONVENTIONAL TPTS

Conventional TPTs are accompanied by gap closing, while unconventional TPTs occur without gap closing. Figure 10 provides some phase diagrams extracted by the method of exact diagonalization [27,31] for the state $j_E = 2$ to illustrate the conventional and unconventional TPTs. Figure 10(a) shows the parity in blue ($P = -1$) and red ($P = +1$); transitions occur when the parity is reversed. These transitions are

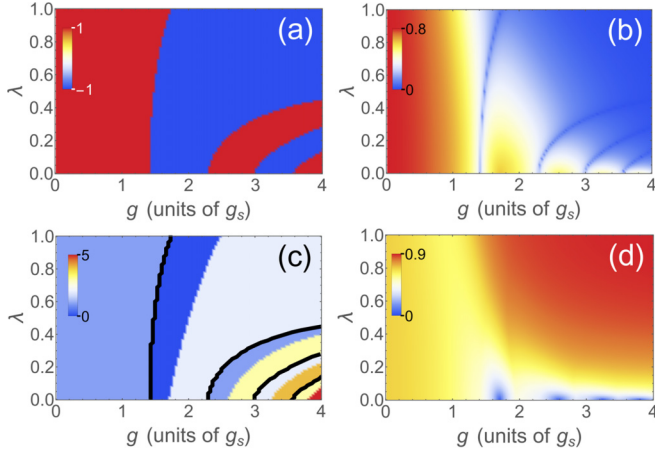


FIG. 10. Phase diagrams in the g - λ plane and unconventional topological phase transitions for state $j_E = 2$. (a) Parity P . (b) First gap Δ_1/ω [plotted by $(\Delta_1/\omega)^{1/4}$ to increase the visibility of the boundaries]. (c) Spin-winding number n_w . The black solid lines mark conventional TPTs at the gap closing boundaries in (a) and (b), while the boundaries between these solid lines are unconventional TPTs without gap closing. (d) Second gap $(\Delta_2/\omega)^{1/2}$. Here $\omega = 0.3\Omega$ and $\chi = 0.5$.

conventional TPTs as the spin-winding number n_w has a jump [Fig. 10(c)] and the gap is closing [Fig. 10(b)]. Apart from these conventional TPTs, in Fig. 10(c) we also see some other TPTs with variations of n_w which do not have a parity reversal or gap closing corresponding to Figs. 10(a) and 10(b). These additional TPTs are unconventional TPTs. The second gap Δ_2 [Fig. 10(d)] along these additional transition boundaries is zero at $\lambda = 0$ but immediately opens once the counterrotating term is turned on by a finite value of λ , which provides an origin tracking for the unconventional TPTs as discussed with Fig. 7 in Sec. VI.

APPENDIX E: COMPARISON OF PERTURBATION AND EXACT DIAGONALIZATION FOR THE OPENING GAP AT FINITE λ

In Fig. 7(f) we have given an example of the opening gap Δ_2 in the presence of the counterrotating term at $\lambda = 0.01$; there the dots mark Δ_2 obtained by perturbation [Eq. (63)]. Here we show the evolution of Δ_2 with respect to λ at a fixed coupling, as illustrated by $g = 1.703g_s$ in Fig. 11. We see that Δ_2 is zero in the absence of the counterrotating term at $\lambda = 0$ but becomes finite and remains open in a finite range of λ . We find that the gap expression (63) by perturbation (blue circles) is working well here up to the anisotropy order $\lambda \sim 0.2$, in comparison with the result of exact diagonalization (green squares) [27,31].

APPENDIX F: EXTRACTING THE WAVE FUNCTION AND SPIN TEXTURE FROM THE SPIN DENSITY

It may be worth mentioning that for an eigenstate of the models in (3) and (4) we can get the wave function and all the spin textures from the spin density (occupation probability of a spin state), which might provide convenience for

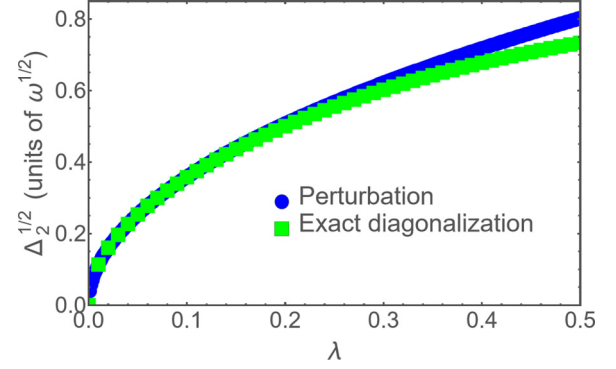


FIG. 11. Comparison of perturbation and exact diagonalization for the opening gap Δ_2 with finite λ at fix $g = 1.703g_s$. Here $\omega = 0.3\Omega$ and $\chi = 0.5$.

experimental measurements for the topological structure. With the notation for the Hamiltonian (3), $\sigma_z = \pm$ represents two flux states in a flux qubit system. The position x and the momentum p can be simulated by the flux and the charge of Josephson junctions in another superconducting circuit system coupled to the qubit system [113,133]. The JCM can also be simulated by adding a gradient magnetic field to the cold-atom system in the trapping potential with spin-orbit coupling [29,138]; in this case the position x is in real space. As shown in Fig. 12 once the spin density $\rho_+^z(x)$ (orange solid line) is available, the wave-function component $\psi_+^z(x)$ (blue dotted line) will be obtained with the amplitude equal to $\sqrt{\rho_+^z(x)}$ and the sign to be reversed across a node, due to the fact that here $\psi_+^z(x)$ is a smooth real function and a cusp is not allowed in quantum mechanics in the absence of potential singularity. There is a free overall sign for $\psi_+^z(x)$, which is however irrelevant. The other wave-function component is simply determined by the parity symmetry as $\psi_-^z(x) = P\psi_+^z(-x)$. In terms of Eqs. (21) and (22), the spin textures of $\langle\sigma_z(x)\rangle$ and $\langle\sigma_x(x)\rangle$ are then both obtained. Here the parity value $P = \pm 1$ can be determined by the sign of the tunneling energy, but the

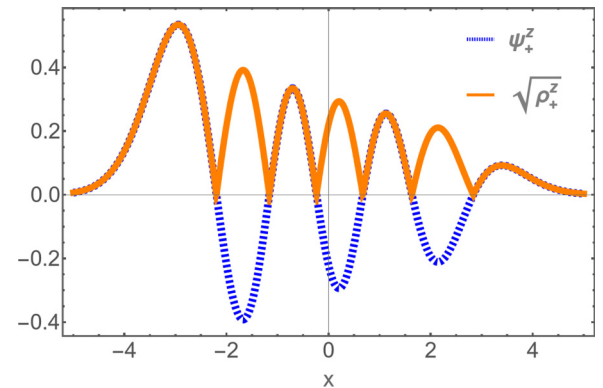


FIG. 12. Extracting the wave function $\psi_+^z(x)$ (blue dotted line) from the spin density $\rho_+^z(x)$ (orange solid line). The wave-function amplitude is determined by $|\psi_+^z(x)| = \sqrt{\rho_+^z(x)}$, while the negative sign in the uncovered dotted sections is picked up by the requirement of a smooth function for the wave function in quantum mechanics. Here the parameters are the same as in Fig. 1.

sign difference of P is reflected only with respect to the $\langle\sigma_z(x)\rangle$ axis for the spin winding in the $\langle\sigma_z(x)\rangle$ - $\langle\sigma_x(x)\rangle$ plane, which

does not affect the topological structure and the absolute spin-winding number.

-
- [1] D. Braak, *Phys. Rev. Lett.* **107**, 100401 (2011).
- [2] E. Solano, *Physics* **4**, 68 (2011).
- [3] A. Le Boité, *Adv. Quantum Technol.* **3**, 1900140 (2020).
- [4] For a review of quantum phase transitions in light-matter interactions see, e.g., J. Liu, M. Liu, Z.-J. Ying, and H.-G. Luo, *Adv. Quantum Technol.* **4**, 2000139 (2021).
- [5] P. Forn-Díaz, L. Lamata, E. Rico, J. Kono, and E. Solano, *Rev. Mod. Phys.* **91**, 025005 (2019).
- [6] A. Frisk Kockum, A. Miranowicz, S. De Liberato, S. Savasta, and F. Nori, *Nat. Rev. Phys.* **1**, 19 (2019).
- [7] Z.-L. Xiang, S. Ashhab, J. Q. You, and F. Nori, *Rev. Mod. Phys.* **85**, 623 (2013); J. Q. You and F. Nori, *Phys. Rev. B* **68**, 064509 (2003).
- [8] A. Wallraff, D. I. Schuster, A. Blais, L. Frunzio, R.-S. Huang, J. Majer, S. Kumar, S. M. Girvin, and R. J. Schoelkopf, *Nature (London)* **431**, 162 (2004).
- [9] C. Ciuti, G. Bastard, and I. Carusotto, *Phys. Rev. B* **72**, 115303 (2005).
- [10] A. A. Anappara, S. De Liberato, A. Tredicucci, C. Ciuti, G. Biasiol, L. Sorba, and F. Beltram, *Phys. Rev. B* **79**, 201303(R) (2009).
- [11] G. Günter, A. A. Anappara, J. Hees, A. Sell, G. Biasiol, L. Sorba, S. De Liberato, C. Ciuti, A. Tredicucci, A. Leitenstorfer, and R. Huber, *Nature (London)* **458**, 178 (2009).
- [12] P. Forn-Díaz, J. Lisenfeld, D. Marcos, J. J. García-Ripoll, E. Solano, C. J. P. M. Harmans, and J. E. Mooij, *Phys. Rev. Lett.* **105**, 237001 (2010).
- [13] T. Niemczyk, F. Deppe, H. Huebl, E. P. Menzel, F. Hocke, M. J. Schwarz, J. J. García-Ripoll, D. Zueco, T. Hümmer, E. Solano, A. Marx, and R. Gross, *Nat. Phys.* **6**, 772 (2010).
- [14] B. Peropadre, P. Forn-Díaz, E. Solano, and J. J. García-Ripoll, *Phys. Rev. Lett.* **105**, 023601 (2010).
- [15] G. Scalari, C. Maissen, D. Turčinková, D. Hagenmüller, S. De Liberato, C. Ciuti, C. Reichl, D. Schuh, W. Wegscheider, M. Beck, and J. Faist, *Science* **335**, 1323 (2012).
- [16] P. Forn-Díaz, J. J. García-Ripoll, B. Peropadre, J. L. Orgiazzi, M. A. Yurtalan, R. Belyansky, C. M. Wilson, and A. Lupascu, *Nat. Phys.* **13**, 39 (2017).
- [17] X. Gu, A. F. Kockum, A. Miranowicz, Y. X. Liu, and F. Nori, *Phys. Rep.* **718–719**, 1 (2017).
- [18] F. Yoshihara, T. Fuse, S. Ashhab, K. Kakuyanagi, S. Saito, and K. Semba, *Nat. Phys.* **13**, 44 (2017).
- [19] A. Bayer, M. Pozimski, S. Schambeck, D. Schuh, R. Huber, D. Bougeard, and C. Lange, *Nano Lett.* **17**, 6340 (2017).
- [20] S. Ashhab, *Phys. Rev. A* **87**, 013826 (2013).
- [21] Z.-J. Ying, M. Liu, H.-G. Luo, H.-Q. Lin, and J. Q. You, *Phys. Rev. A* **92**, 053823 (2015).
- [22] M.-J. Hwang, R. Puebla, and M. B. Plenio, *Phys. Rev. Lett.* **115**, 180404 (2015).
- [23] M.-J. Hwang and M. B. Plenio, *Phys. Rev. Lett.* **117**, 123602 (2016).
- [24] J. Larson and E. K. Irish, *J. Phys. A: Math. Theor.* **50**, 174002 (2017).
- [25] M. Liu, S. Chesi, Z.-J. Ying, X. Chen, H.-G. Luo, and H.-Q. Lin, *Phys. Rev. Lett.* **119**, 220601 (2017).
- [26] Z.-J. Ying, L. Cong, and X.-M. Sun, *J. Phys. A: Math. Theor.* **53**, 345301 (2020).
- [27] Z.-J. Ying, *Phys. Rev. A* **103**, 063701 (2021).
- [28] Z.-J. Ying, *Adv. Quantum Technol.* **5**, 2100088 (2022); **5**, 2270013 (2022).
- [29] Z.-J. Ying, *Adv. Quantum Technol.* **5**, 2100165 (2022).
- [30] Z.-J. Ying, *Adv. Quantum Technol.* **6**, 2200068 (2023); **6**, 2370011 (2023).
- [31] Z.-J. Ying, *Adv. Quantum Technol.* **6**, 2200177 (2023); **6**, 2370071 (2023).
- [32] R. Grimaudo, A. S. Magalhães de Castro, A. Messina, E. Solano, and D. Valenti, *Phys. Rev. Lett.* **130**, 043602 (2023).
- [33] R. Grimaudo, D. Valenti, A. Sergi, and A. Messina, *Entropy* **25**, 187 (2023).
- [34] F. A. Wolf, M. Kollar, and D. Braak, *Phys. Rev. A* **85**, 053817 (2012).
- [35] S. Felicetti and A. Le Boité, *Phys. Rev. Lett.* **124**, 040404 (2020).
- [36] S. Felicetti, M.-J. Hwang, and A. Le Boité, *Phys. Rev. A* **98**, 053859 (2018).
- [37] U. Alushi, T. Ramos, J. J. García-Ripoll, R. Di Candia, and S. Felicetti, *PRX Quantum* **4**, 030326 (2023).
- [38] E. K. Twyeffort Irish and A. D. Armour, *Phys. Rev. Lett.* **129**, 183603 (2022).
- [39] E. K. Irish and J. Gea-Banacloche, *Phys. Rev. B* **89**, 085421 (2014).
- [40] D. Braak, Q. H. Chen, M. T. Batchelor, and E. Solano, *J. Phys. A: Math. Theor.* **49**, 300301 (2016).
- [41] A. J. Maciejewski, M. Przybylska, and T. Stachowiak, *Phys. Lett. A* **378**, 3445 (2014); **379**, 1503 (2015).
- [42] H. P. Eckle and H. Johannesson, *J. Phys. A: Math. Theor.* **50**, 294004 (2017); **56**, 345302 (2023).
- [43] Y.-F. Xie, L. Duan, and Q.-H. Chen, *J. Phys. A: Math. Theor.* **52**, 245304 (2019).
- [44] Y.-Q. Shi, L. Cong, and H.-P. Eckle, *Phys. Rev. A* **105**, 062450 (2022).
- [45] Q.-T. Xie, S. Cui, J.-P. Cao, L. Amico, and H. Fan, *Phys. Rev. X* **4**, 021046 (2014).
- [46] H.-J. Zhu, K. Xu, G.-F. Zhang, and W.-M. Liu, *Phys. Rev. Lett.* **125**, 050402 (2020).
- [47] S. Felicetti, D. Z. Rossatto, E. Rico, E. Solano, and P. Forn-Díaz, *Phys. Rev. A* **97**, 013851 (2018).
- [48] S. Felicetti, J. S. Pedernales, I. L. Egusquiza, G. Romero, L. Lamata, D. Braak, and E. Solano, *Phys. Rev. A* **92**, 033817 (2015).
- [49] L. Garbe, I. L. Egusquiza, E. Solano, C. Ciuti, T. Coudreau, P. Milman, and S. Felicetti, *Phys. Rev. A* **95**, 053854 (2017).
- [50] R. J. A. Rico, F. H. Maldonado-Villamizar, and B. M. Rodríguez-Lara, *Phys. Rev. A* **101**, 063825 (2020).
- [51] L. Garbe, M. Bina, A. Keller, M. G. A. Paris, and S. Felicetti, *Phys. Rev. Lett.* **124**, 120504 (2020).

- [52] L. Garbe, O. Abah, S. Felicetti, and R. Puebla, *Phys. Rev. Res.* **4**, 043061 (2022).
- [53] T. Ilias, D. Yang, S. F. Huelga, and M. B. Plenio, *PRX Quantum* **3**, 010354 (2022).
- [54] Z.-J. Ying, S. Felicetti, G. Liu, and D. Braak, *Entropy* **24**, 1015 (2022).
- [55] A. Le Boité, M.-J. Hwang, H. Nha, and M. B. Plenio, *Phys. Rev. A* **94**, 033827 (2016).
- [56] A. Ridolfo, M. Leib, S. Savasta, and M. J. Hartmann, *Phys. Rev. Lett.* **109**, 193602 (2012).
- [57] Z.-M. Li, D. Ferri, D. Tilbrook, and M. T. Batchelor, *J. Phys. A: Math. Theor.* **54**, 405201 (2021).
- [58] M. Liu, Z.-J. Ying, J.-H. An, and H.-G. Luo, *New J. Phys.* **17**, 043001 (2015).
- [59] L. Cong, X.-M. Sun, M. Liu, Z.-J. Ying, and H.-G. Luo, *Phys. Rev. A* **95**, 063803 (2017).
- [60] L. Cong, X.-M. Sun, M. Liu, Z.-J. Ying, and H.-G. Luo, *Phys. Rev. A* **99**, 013815 (2019).
- [61] G. Liu, W. Xiong, and Z.-J. Ying, *Phys. Rev. A* **108**, 033704 (2023).
- [62] K. K. W. Ma, *Phys. Rev. A* **102**, 053709 (2020).
- [63] Q.-H. Chen, C. Wang, S. He, T. Liu, and K.-L. Wang, *Phys. Rev. A* **86**, 023822 (2012).
- [64] L. Duan, Y.-F. Xie, D. Braak, and Q.-H. Chen, *J. Phys. A* **49**, 464002 (2016).
- [65] Y.-Y. Zhang, *Phys. Rev. A* **94**, 063824 (2016).
- [66] Z. Lü, C. Zhao, and H. Zheng, *J. Phys. A: Math. Theor.* **50**, 074002 (2017).
- [67] L.-T. Shen, Z.-B. Yang, H.-Z. Wu, and S.-B. Zheng, *Phys. Rev. A* **95**, 013819 (2017).
- [68] Y. Yan, Z. Lü, L. Chen, and H. Zheng, *Adv. Quantum Technol.* **6**, 2200191 (2023).
- [69] X. Chen, Z. Wu, M. Jiang, X.-Y. Lü, X. Peng, and J. Du, *Nat. Commun.* **12**, 6281 (2021).
- [70] X. Y. Lü, L. L. Zheng, G. L. Zhu, and Y. Wu, *Phys. Rev. Appl.* **9**, 064006 (2018).
- [71] B.-L. You, X.-Y. Liu, S.-J. Cheng, C. Wang, and X.-L. Gao, *Acta Phys. Sin.* **70**, 100201 (2021).
- [72] M. T. Batchelor and H.-Q. Zhou, *Phys. Rev. A* **91**, 053808 (2015).
- [73] Q. Xie, H. Zhong, M. T. Batchelor, and C. Lee, *J. Phys. A: Math. Theor.* **50**, 113001 (2017).
- [74] S. Bera, S. Florens, H. U. Baranger, N. Roch, A. Nazir, and A. W. Chin, *Phys. Rev. B* **89**, 121108(R) (2014).
- [75] L. Yu, S. Zhu, Q. Liang, G. Chen, and S. Jia, *Phys. Rev. A* **86**, 015803 (2012).
- [76] T. Liu, M. Feng, W. L. Yang, J. H. Zou, L. Li, Y. X. Fan, and K. L. Wang, *Phys. Rev. A* **88**, 013820 (2013).
- [77] J. Peng, E. Rico, J. Zhong, E. Solano, and I. L. Egusquiza, *Phys. Rev. A* **100**, 063820 (2019).
- [78] J. Casanova, R. Puebla, H. Moya-Cessa, and M. B. Plenio, *npj Quantum Inf.* **4**, 47 (2018).
- [79] D. Braak, *Symmetry* **11**, 1259 (2019).
- [80] V. V. Mangazeev, M. T. Batchelor, and V. V. Bazhanov, *J. Phys. A: Math. Theor.* **54**, 12LT01 (2021).
- [81] Z.-M. Li and M. T. Batchelor, *Phys. Rev. A* **103**, 023719 (2021).
- [82] C. Reyes-Bustos, D. Braak, and M. Wakayama, *J. Phys. A: Math. Theor.* **54**, 285202 (2021).
- [83] J. Larson and T. Mavrogordatos, *The Jaynes-Cummings Model and Its Descendants* (IOP, London, 2021).
- [84] L. Cong, S. Felicetti, J. Casanova, L. Lamata, E. Solano, and I. Arrazola, *Phys. Rev. A* **101**, 032350 (2020).
- [85] A. L. Grimsmo and S. Parkins, *Phys. Rev. A* **87**, 033814 (2013).
- [86] A. L. Grimsmo and S. Parkins, *Phys. Rev. A* **89**, 033802 (2014).
- [87] C. A. Downing and A. J. Toghiani, *Sci. Rep.* **12**, 11630 (2022).
- [88] L. D. Landau, *Zh. Eksp. Teor. Fiz.* **7**, 19 (1937).
- [89] D. J. Thouless, M. Kohmoto, M. P. Nightingale, and M. den Nijs, *Phys. Rev. Lett.* **49**, 405 (1982).
- [90] J. M. Kosterlitz and D. J. Thouless, *J. Phys. C* **6**, 1181 (1973).
- [91] F. D. M. Haldane, *Phys. Lett.* **93A**, 464 (1983).
- [92] F. D. M. Haldane, *Phys. Rev. Lett.* **50**, 1153 (1983).
- [93] Z.-C. Gu and X.-G. Wen, *Phys. Rev. B* **80**, 155131 (2009).
- [94] X.-G. Wen, *Rev. Mod. Phys.* **89**, 041004 (2017).
- [95] S. Sachdev, *Quantum Phase Transitions*, 2nd ed. (Cambridge University Press, Cambridge, 2011).
- [96] I. I. Rabi, *Phys. Rev.* **51**, 652 (1937).
- [97] H.-P. Eckle, *Models of Quantum Matter* (Oxford University Press, Oxford, 2019).
- [98] Z.-J. Ying, M. Cuoco, C. Noce, and H.-Q. Zhou, *Phys. Rev. Lett.* **100**, 140406 (2008).
- [99] Z.-J. Ying, M. Cuoco, C. Noce, and H.-Q. Zhou, *Phys. Rev. B* **76**, 132509 (2007).
- [100] Z.-J. Ying, M. Cuoco, C. Noce, and H.-Q. Zhou, *Phys. Rev. B* **78**, 104523 (2008); **74**, 012503 (2006); **74**, 214506 (2006).
- [101] V. M. Stojanović, *Phys. Rev. B* **101**, 134301 (2020).
- [102] V. M. Stojanović, *Phys. Rev. Lett.* **124**, 190504 (2020).
- [103] V. M. Stojanović, *Phys. Rev. A* **103**, 022410 (2021).
- [104] M. Z. Hasan and C. L. Kane, *Rev. Mod. Phys.* **82**, 3045 (2010).
- [105] R. Yu, W. Zhang, H.-J. Zhang, S.-C. Zhang, X. Dai, and Z. Fang, *Science* **329**, 61 (2010).
- [106] H. Zou, E. Zhao, X.-W. Guan, and W. V. Liu, *Phys. Rev. Lett.* **122**, 180401 (2019).
- [107] W. Chen and A. P. Schnyder, *New J. Phys.* **21**, 073003 (2019).
- [108] Z.-X. Li, Y. Cao, X. R. Wang, and P. Yan, *Phys. Rev. Appl.* **13**, 064058 (2020).
- [109] Y. Che, C. Gneiting, T. Liu, and F. Nori, *Phys. Rev. B* **102**, 134213 (2020).
- [110] A. Amaricci, J. C. Budich, M. Capone, B. Trauzettel, and G. Sangiovanni, *Phys. Rev. Lett.* **114**, 185701 (2015).
- [111] C.-Z. Chen, J. Qi, D.-H. Xu, and X. C. Xie, *Sci. China Phys. Mech. Astron.* **64**, 127211 (2021).
- [112] E. T. Jaynes and F. W. Cummings, *Proc. IEEE* **51**, 89 (1963).
- [113] J. E. Mooij, T. P. Orlando, L. Levitov, L. Tian, C. H. van der Wal, and S. Lloyd, *Science* **285**, 1036 (1999).
- [114] F. Nagasawa, D. Frustaglia, H. Saarikoski, K. Richter, and J. Nitta, *Nat. Commun.* **4**, 2526 (2013).
- [115] Z.-J. Ying, P. Gentile, C. Ortix, and M. Cuoco, *Phys. Rev. B* **94**, 081406(R) (2016).
- [116] Z.-J. Ying, M. Cuoco, C. Ortix, and P. Gentile, *Phys. Rev. B* **96**, 100506(R) (2017).
- [117] Z.-J. Ying, P. Gentile, J. P. Baltanás, D. Frustaglia, C. Ortix, and M. Cuoco, *Phys. Rev. Res.* **2**, 023167 (2020).
- [118] P. Gentile, M. Cuoco, O. M. Volkov, Z.-J. Ying, I. J. Vera-Marun, D. Makarov, and C. Ortix, *Nat. Electron.* **5**, 551 (2022).

- [119] Y.-J. Lin, K. Jiménez-García, and I. B. Spielman, *Nature (London)* **471**, 83 (2011).
- [120] V. Galitski and I. B. Spielman, *Nature (London)* **494**, 49 (2013).
- [121] G. Dresselhaus, *Phys. Rev.* **100**, 580 (1955).
- [122] Y. A. Bychkov and E. I. Rashba, *J. Phys. C* **17**, 6039 (1984).
- [123] S. Nadj-Perge, I. K. Drozdov, J. Li, H. Chen, S. Jeon, J. Seo, A. H. MacDonald, B. A. Bernevig, and A. Yazdani, *Science* **346**, 602 (2014).
- [124] S. Jeon, Y. Xie, J. Li, Z. Wang, B. A. Bernevig, and A. Yazdani, *Science* **358**, 772 (2017).
- [125] Q.-X. Lv, Y.-X. Du, Z.-T. Liang, H.-Z. Liu, J.-H. Liang, L.-Q. Chen, L.-M. Zhou, S.-C. Zhang, D.-W. Zhang, B.-Q. Ai, H. Yan, and S.-L. Zhu, *Phys. Rev. Lett.* **127**, 136802 (2021).
- [126] E. K. Irish, J. Gea-Banacloche, I. Martin, and K. C. Schwab, *Phys. Rev. B* **72**, 195410 (2005).
- [127] I. Pietikäinen, S. Danilin, K. S. Kumar, A. Vepsäläinen, D. S. Golubev, J. Tuorila, and G. S. Paraoanu, *Phys. Rev. B* **96**, 020501(R) (2017).
- [128] Y. Wang, W.-L. You, M. Liu, Y.-L. Dong, H.-G. Luo, G. Romero, and J. Q. You, *New J. Phys.* **20**, 053061 (2018).
- [129] G. Wang, R. Xiao, H. Z. Shen, and K. Xue, *Sci. Rep.* **9**, 4569 (2019).
- [130] J. Casanova, G. Romero, I. Lizuain, J. J. García-Ripoll, and E. Solano, *Phys. Rev. Lett.* **105**, 263603 (2010).
- [131] A. Stokes and A. Nazir, *Nat. Commun.* **10**, 499 (2019).
- [132] J.-F. Huang, J.-Q. Liao, and L.-M. Kuang, *Phys. Rev. A* **101**, 043835 (2020).
- [133] J. Q. You, Y. Nakamura, and F. Nori, *Phys. Rev. B* **71**, 024532 (2005).
- [134] Z.-J. Ying, *Adv. Quantum Technol.* **7**, 2400053 (2024).
- [135] Y. Li, L. P. Pitaevskii, and S. Stringari, *Phys. Rev. Lett.* **108**, 225301 (2012).
- [136] A. Bermudez, M. A. Martin-Delgado, and E. Solano, *Phys. Rev. A* **76**, 041801(R) (2007).
- [137] T. Ma and S. Wang, *Topological Phase Transitions* (HAL, Lyon, 2017).
- [138] Z.-J. Ying (unpublished).